November 2022| Volume 01 | Issue 03 | Pages 19-43

Future Energy
Open Access Journal
ISSN 2832-0328

Journal homepage: https://fupubco.com/fuen

https://doi.org/10.55670/fpll.fuen.1.3.4

Future Publishing LLC

Review

Charge transport materials, bismuth and copper-based perovskite solar cells: A review

Ankit Stephen Thomas*

Department of Chemical Engineering, National Institute of Technology Karnataka, Surathkal, India

ARTICLE INFO

Article history:
Received 05 May 2022
Received in revised form
08 June 2022
Accepted 13 June 2022

Keywords:
Perovskite solar cells, Charge transport materials, photovoltaics, Bi and Cu-based PSCs, third-generation solar cells

*Corresponding author
Email address:
ankitsthomas@gmail.com

DOI: 10.55670/fpll.fuen.1.3.4

ABSTRACT

Improving perovskite solar cell (PSC) efficiencies would not have been possible without discovering and incorporating novel materials. More significant than materials usage is the compatibility of various material components in the entire device. Charge transport materials have been at the heart of this discussion to decide a PSC's functioning fundamentally. This review highlights various high-efficiency examples using alternate charge transport materials, bringing us one step closer to commercializing this technology. The article also elaborates on recent innovations in Bismuth and Copper-based PSCs. These are possible candidates to replace the conventional materials used in a standard PSC and affirmatively yield favorable results through extensive research.

1. Introduction

Due to the enormous jump (3% to ~25%) in Power Conversion Efficiencies (PCEs) of Perovskite Solar Cells (PSCs) in the past decade, it has been one of the modern photovoltaic technologies. However, using noble metals as electrodes and expensive charge transporting materials have shown little to no good for PSC's stability. The cost of procurement, low stability of devices, high fabrication costs, and developed technologies require constant innovation and modification. The rising levels of lead toxicity are raising a large concern amongst the photovoltaic community. It is essential to find alternative metals that can replace the role of Pb in traditional perovskite solar cells with a robust, stable, efficient, and commercial metal. Copper and Bismuth-based PSCs are excellent candidates for PSCs due to their unique structural and optoelectronic properties. However, these materials' usage in PSCs has not yielded sufficient efficiencies. This review will examine the alternative organic charge transport materials that provide reasonable efficiencies. We shall also study the works of research groups that have made considerable progress in Bi and Cu-based PSCs which can be the next step for commercialization. PSCs have an effortless fundamental working mechanism. The incident radiation generates photoexcited electrons and holes in the perovskite active layer. These generated charge carriers are separated with the help of respective charge transport materials, namely hole and electron transport materials or layers. These are then transported to their respective electrodes to travel through the external circuit and power the load. Electron transport materials (ETM), as the name suggests, have a significant function of transporting electrons and, at the same time, blocking holes. The process of recombination needs to be inhibited as it severely impacts the device's performance, and ETMs play a considerable role in mitigating this. While appointing an ETM, one needs to analyze several factors such as electron mobility, electron transport lifetime, material compatibility, stability, and other auxiliary factors. Hole transport materials (HTM) play a vital role in transporting photogenerated holes and blocking electrons. These layers are significant as they dictate the device's electrode stability, open-circuit voltage (V_{oc}), and charge carrier mobility. Optimizing the HTM right from the morphology level upwards can influence the stability and performance and positively contribute to the device. Bismuth and copper-based PSCs have been recently actively considered for perovskite components due to their abundant sources, superior stability, and non-toxic and appropriate optoelectronic properties. However, their wide bandgaps, high binding energies, and consequently limited efficiency values have led these materials to further research and limited applications. This article focuses on specific examples of how various scientists and research groups have globally

developed alternative charge transport materials to produce high-efficiency devices. Moreover, the article shall also throw some light on Bi and Cu-based PSCs being used in perovskite and charge transport components to produce reasonable efficiency values.

2. Results and Discussion

2.1 Carbon and P3HT PSCs

Carbon-based PSCs (C-PSCs) have paved the way for such a demand to produce stable, efficient, cheap, and compatible PSCs. PSCs with Carbon electrodes have shown to be of exceptional photovoltaic performance. There has been no requirement for HTMs due to superior stability in some instances. C-PSCs and TiO_2 as an ETM require high thermal annealing temperatures. Thus, finding alternative ETMs that can complement Carbon electrodes is essential. ZnO is a popular option due to its high electron mobility (205-300 $cm^2V^{-1}s^{-1}$) and has low-temperature preparation procedures. When ZnO is incorporated with C-PSCs, the highest reported PCE is only 13.6%. The mass usage of C-PSCs is limited due to the absence of HTMs. There is no appropriate material whose energy band aligns with the Carbon electrode ideally, which causes excessive charge accumulation at the Carbon electrode. This impedes charge transfer and consequently affects the performance of the device. Hence, it is required to develop an efficient HTM that can bridge this energy gap and improve the short circuit current (J_{sc}), open-circuit voltage (V_{oc}), fill factor (FF), PCE, and thus the performance. Using organic HTMs like 2,2',7,7'-Tetrakis[N,N-di(4-methoxyphenyl)amino]-9,9'-spirobifluorene (spiro-OMETAD) and Poly[bis(4-phenyl)(2,4,6-trimethylphenyl)amine Poly(triarylamine) (PTAA) are few conventionally used HTMs. However, their low hole mobilities and expensive nature are not feasible to use these materials in the long run. Using additives can improve the auxiliary properties of the device, but it has been reported that additives produce unstable devices. Poly(3-hexylthiophene-2,5-diyl) (P3HT) is a polymer that can produce exceptional devices due to its solution processing capability, low cost, and larger scope for commercial production. The hydrophobic nature of P3HT improves the moisture stability of the device. It thus impacts the long-term stability of the device. Moreover, P3HT has high hole mobility (0.1 cm^2V^{-1}) and has a bandgap of 1.9-2.0 eV, which suitably aligns with the solar spectrum. In this work, Junjun Jin and coworkers show how Carbon-based PSCs are suitable contenders for high-performance, good stability, and low-cost devices using suitable modifications and alterations [1]. The architecture of the PSC used in this case is FTO/ZnO/$CH_3NH_3PbI_3$/P3HT/C, which has appropriate energy band alignment and, consequently, reduced charge recombination probability. The thicknesses of ZnO, $CH_3NH_3PbI_3$ ($MAPbI_3$), and P3HT are 50 nm, 610 nm, and 43 nm, respectively. Different concentrations of the precursor solutions were used to find the optimum P3HT thickness. The ideal thickness is required for optimum hole collection. While exploring the different concentrations of P3HT precursor solution, it is observed that the perovskite surface coverage for concentrations below 10 mg/mL. When the concentration gradually increases to 12 mg/mL, the surface coverage is more uniform, thus indicating more uniform films. The obtained grain size of the perovskite film is in the range of 300 - 400 nm. Moreover, on the complete deposition of P3HT on the perovskite film, there was no change in morphology. This indicates that both the films are compatible with each other, and there is no damage caused. Figure 1 shows the energy band alignment of the device employing a ZnO ETM, P3HT ETM, and Carbon electrode.

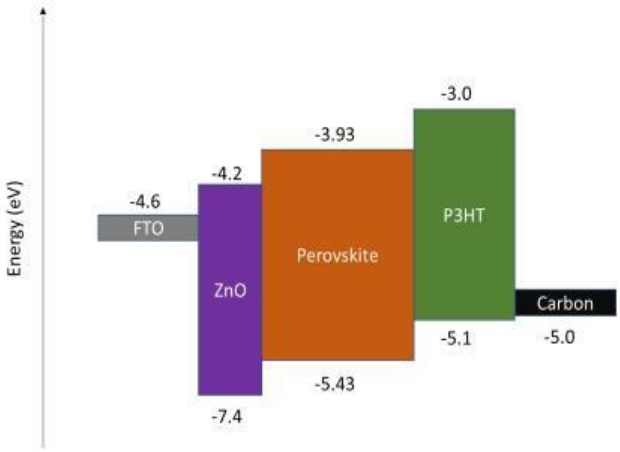

Figure 1. Energy band alignment of the device

The photovoltaic performance is recorded for different concentrations of the P3HT precursor solution. When the concentration is less than 8 mg/mL, the PCE is lower than devices without the P3HT layer. The P3HT film impacts the Jsc but has a negligible impact on the V_{oc}. As the concentration is increased to 10 mg/mL, there is a rapid improvement in J_{sc} and V_{oc}. When the concentration reaches 12 mg/mL, the optimum performance is attained as J_{sc} = 19.87 mA/cm^2, V_{oc} = 1.03 V, FF = 68.89% and a PCE = 14.10%. However, as the concentration increases to 15 mg/mL, the performance decreases. The increased performance can be justified by the HTM having efficient hole transportation properties, decreasing charge recombination, and efficiently blocking electrons. Table 1 shows a comparative analysis of devices with and without P3HT.

Table 1. Device Performance with and without P3HT

Device	PCE	J_{sc}	V_{oc}	FF
Without P3HT	11.69	18.48	0.97	65.21
With P3HT	16.05	20.62	1.02	76.31

The following results can be summarized through Electrochemical Impedance Spectra (EIS). The Rs increase as P3HT precursor concentration increases. When concentration is lesser than 15 mg/mL, the R_{tr} and R_{rec} increase with the concentration of P3HT solution. An increase in Rtr indicates the interface resistance of charges between the perovskite/P3HT layer. An increase in R_{rec} indicates a decrease in charge recombination. The increase in R_{tr} and R_s is bad for the device. However, in this case, the substantial increase of R_{rec} compensates for the cumulative

effects of the latter. This produces more V_{oc}, J_{sc}, FF, and thus, more PCE. Again as concentration increases to 15 mg/mL, the R_{rec} tends to decrease, indicating that the optimum concentration for the P3HT layer is 12 mg/mL. An optimized device of the same C-PSC with P3HT is developed to obtain V_{oc} = 1.02 V, J_{sc} = 20.62 mA/cm^2, FF = 76.31% and PCE = 16.05%. The FF achieved, in this case, can be compared to that of metal electrodes. Photoluminescence (PL) measurements are taken to study the charge transport dynamics.

$MAPbI_3$/Glass and P3HT/$MAPbI_3$/Glass are the two devices for taking the measurements. The PL spectrum of $MAPbI_3$ shows the regular strong luminescence at 782 nm. The PL quenching phenomenon can be observed in the P3HT device as the PL intensity is very sensitive to the P3HT HTM. This quenching shows that the photo-generated charge carriers are rapidly transferred to the P3HT layer from the perovskite layer. From the time-resolved photoluminescence measurements, the device without P3HT had T_1 = 61.6 ns, T_2 = 15.6 ns, and the device with P3HT had T_1 = 149.6 ns, T_2 = 27.7 ns, which indicates a greater charge lifetime and effective charge transfer at the perovskite/P3HT interface. Fifty devices were made to test the reproducibility of C-PSCs. Increasing the P3HT layer can improve the device's J_{sc}, V_{oc}, FF, and PCE with excellent repeatability. The device shows a steady-state reading under constant illumination. The current shot was 17.92 mA/cm^2 at 0.78 V bias under 100 mW/cm^2 with a PCE of 13.97%. The device delivers a stable output after 150 seconds of constant illumination, showing that it has stable properties under direct light illumination. The device is stored under 25^{o}C-35^{o}C with 35-50% RH under ambient conditions for 1200 hours without encapsulation. It retained 90% of its initial PCE, indicating good stability. Lastly, the large contact angle with water of P3HT shows that its hydrophobic properties can protect the perovskite active layer from degrading rapidly and improve the device's stability.

2.2 Fluorinated Aliphatic Amines using Interfacial Engineering

The primary reason for the degradation of PSCs is the instability causes. These causes can be related to the grain size boundaries and defective surface nature that allow the permeation of moisture to destroy the performance of PSCs further and accelerate its degradation. Additive treatments can supplement the performance of PSCs like, as done by Dai and coworkers, who used C60 as an additive layer [2]. Similarly, Zhang and coworkers developed an antisolvent treatment. In both cases, the stability of the devices increased. However, the addition of additives can be highly cost-intensive, which will harm the long-term commercialization or operation of the device. Using hydrophobic molecules like thiols and polystyrene improves the moisture stability of the device considerably. However, reports have suggested that once these molecules are incorporated into the device as a blocking layer or into any of the layers, the charge transport properties of these materials are suppressed, which further impacts the performance. The need to develop layers that provide a passivation effect but at the same time offer a modification of surface features is of utmost importance. In this section, Shuai Zhao and coworkers developed a set of fluorinated amines as a barrier layer/additive layer known to modulate the perovskite charge-transporting properties and hydrophobicity [3]. In this case, three fluorinated aliphatic amines are used 2,2,2-trifluoroethylamine iodide, 1H,1Hheptafluorobutylamine iodide, and 1H,1H-perfluoroctylamine iodide, and the resulted films are represented as 2-HI-PVK, 4-HI-PVK, and 8-HI-PVK, respectively. The water contact angle measurements were taken to study the hydrophobicity. The angles were 40^o, 67^o, 71^o, and 97^o for unmodified perovskite, 2-HI-PVK, 4-HI-PVK, and 8-HI-PVK, respectively. Thus, we can conclude that the increasing number of -CF2- groups can increase the hydrophobicity significantly. However, it has been studied that an increasing number of fluorinated aliphatic amine groups increases hydrophobicity and lipophobicity. This makes it hard for PCBM to be deposited on the surface of the perovskite film. Hence, only the 2-HI-PVK and 4-HI-PVK films are being considered in further discussion. On conducting the XRD analysis, all films showed two intense peaks at 14.2^o and 28.4^o and small peaks attributed to MAPbI3. In the case of unmodified perovskites, a peak is observed at 12.8^o, associated with PbI_2 impurities. This peak is not observed in the case of the amine-based perovskites, thus showing that these films are more stable and uniform. SEM analysis shows that all the films show a similar morphology. However, in the case of amines, the grain size becomes more extensive. As the grain size increases, the grain boundary associated defects decrease, and Ostwald ripening recrystallization can be observed in this case during the annealing process. Moreover, the large grain size can even reduce charge recombination, thus improving photovoltaic performance. The AFM results depict the surface roughness. The RMS roughness of the film is reduced considerably where 11.20 nm, 9.95 nm, and 9.84 nm values were obtained for unmodified, 2-HI-PVK and 4-HI-PVK films, respectively. The smoother the films, the easier the charge transport and permitting efficient charge transport and separation for better performance. Forty devices of each type were produced to record all the material types' best and average efficiencies. The photovoltaic performance was recorded by a solar simulator at AM 1.5G, 100 W/m^2. The device's architecture is FTO/PEDOT:PSS/Perovskite/PC61BM/BCP/Ag. This was used as the reference device. The modified fluorinated aliphatic amines were placed as a barrier layer between the ETM/perovskite interface. The low work function of PEDOT:PSS is responsible for the reduced V_{oc} values, which consequently give rise to lower PCE values. The PCE values obtained are 12.23%, 12.76%, and 13.88% for the unmodified, 2-HI-PVK, and 4-HI-PVK devices. The V_{oc} and FF values are unchanged. Thus, PCE values can be related to the improved J_{sc} values due to the efficient charge transport among materials and interfaces.

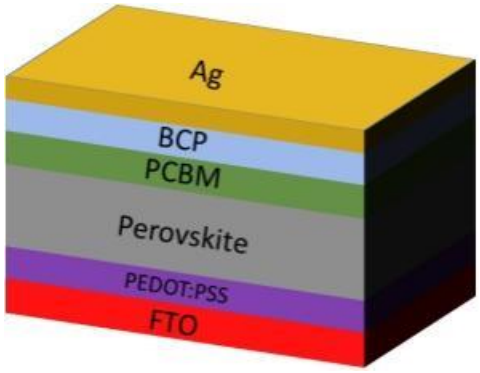

Figure 2. PSC Device Architecture

The Hysteresis Factor or Hysteresis Index (HI) is calculated using the formula below:

$$HI = ((PCE_{forward} - PCE_{revrse})/PCE_{reverse})$$

Figure 2 shows the PSC architecture with a device having an interfacial engineering element.

The HI value is calculated to be 0.65%, 0.93%, and 1.09% for the control, 2-HI-PVK, and 4-HI-PVK devices, respectively. The increased HI values can be related to the electronegative solid character of fluorocarbon groups which cause electron flooding near the interface of the perovskite/ETM layer, thus the cause of hysteresis. The trap-filled density is calculated using the trap-filled limit voltage (V_{TFL}). The V_{TFL} values significantly decrease as we proceed from the control to the amine-based film. This shows the reduced trap density in each of the corresponding films. The IPCE measurements are taken to study incident photon-to-electron conversion efficiency. The IPCE values are higher than the control device, agreeing with the J-V analysis. Notably, comparing the three devices, the steady-state current value reaches quicker for the amine-based device than the control device. This can be related to the modified films' better charge extraction, separation, and collection efficiency, which shows faster carrier transport. The stability of the devices was studied under 50% RH for ten days. The PCE of the control device was found to be less than 50% of its initial efficiency in 3 days. The 4-HI-PVK device reduces to 15% of its initial PCE after ten days, and the 2-HI-PVK device reduces to 20% after ten days. These results indicate how the modification of the film improves the stability properties significantly. The charge transfer and dynamics in the device are studied by photoluminescence emission spectra of the perovskite materials, along with TRPL measurements. All films show an emission spectrum of 790 nm. However, the PL intensity increases from the control film to the modified film. The PL intensity for 4-HI-PVK is nearly 1.5 times stronger than that of the control film. These results indicate that the recombination of charge carriers is highly suppressed. The reduced number of grain boundary defects can improve charge transport and extraction. The TRPL results fit a bi-exponential model to give the time constant T_1 and T_2. The shorter time constant is related to defect-assisted recombination. The longer time constant is related to intrinsic radiative recombination. The T_1 values decrease when moving from the control film to the modified films, thus showing that nonradiative recombination is highly reduced due to the large grain sizes and reduced grain boundary defects. The Electrostatic Potential (ESP) analysis is conducted. These results show that the negative charge is localized around the electronegative F atom. This further show that the F ions can form a coordinate bond between uncoordinated Pb^{2+} atoms to give rise to improved molecular interactions. Therefore, the fluorine ions in the 2,2,2-trifluoroethylamine iodide or 1H,1H-heptafluorobutylamine iodide can passivate the iodide vacancies and reduce the nonradiative recombination. From the T_2 values, a faster decay is observed for modified films, which shows faster charge collection and higher electron-withdrawing capacity attributed to the electronegative fluorocarbon groups. Moreover, analyzing the surface energy levels of the modified perovskite film, we can see an n-type characteristic for the modified films, which facilitates electron collection, separation, and transportation to maintain charge neutrality in the film. These modifications increase band bending, reduce band difference between the perovskite/ETM interface, and improve charge transport. The EIS measurements of the control, 2-HI-PVK, and 4-HI-PVK films are analyzed. At high frequencies (>500 Hz), we can observe a Nyquist plot to develop an equivalent circuit model to relate the charge transport and recombination process. The R_{rec} values are 26.65, 77.69, and 103.7 Ω for the control, 2-HI-PVK, and 4-HI-PVK films, respectively. The higher values of R_{rec} indicate the reduced probability of recombination of charge carriers, which is also in agreement with the PL analysis measurements. From this study, the modified film of hydrophobic fluorinated aliphatic amines can significantly reduce charge recombination, improve charge transport, resist moisture penetration, and provide a possible mechanism for passivation, opening new ventures for commercial PSCs [4].

2.3 Conjugated Polyelectrolytes as HTM in PSCs

PEDOT: PSS is a conventional HTM used to produce high-efficiency PSCs. However, the acidic nature of PEDOT: PSS can easily corrode the FTO or ITO layer used in the device. Hence, using alternative HTMs is often considered. Inorganic HTMs like NiO_x, V_2O_5, and CuI have been used in PSCs, but their rigid nature restricts them from mass commercialization. Using organic HTMs like small molecules and polymers has tremendous advantages due to its flexible nature, tunable properties, and simple molecular design and thus can be studied easily. Small molecule HTMs can partially dissolve in solvents used for perovskite solutions. This makes it hard to study or comprehend their feasibility in the short or long run. Using conjugated polymers has often formed an exceptional film that can generate excellent devices due to its superior device coverage and appropriate wettability, a much-needed feature for mass-produced devices. Conjugated Polyelectrolyte (CPE) with organic cations can often compliment the $CH_3NH_3^+$ (MA^+), FA^+ or GA^+ ions used in PSCs. Such a configuration is never used in any other photovoltaic technology. Using organic cations similar to perovskite materials can generate strong interactions and improve PCE levels to a greater extent. In the past, it has been reported that small molecules with ammonium ions were able to passivate the surface defects at the perovskite layer. In this section, Luozheng Zhang and coworkers developed a polymer with a backbone 2,5-dialkoxy-1,4-phenylene unit and thiophene unit. The side-chain is end-capped by $-SO_3$-MA^+, termed TB(MA) [5]. TB(MA) structure is fabricated by Stille Coupling polymerization followed by ion-exchange mechanisms. The obtained work function of TB(MA) is 5.12 eV on an ITO substrate through ultraviolet photoelectron spectroscopy (UPS). The value of PEDOT: PSS obtained through such a measurement is 5.11 eV, indicating that both the materials are comparable in nature and can work as HTMs with appropriate energy band alignment. The transmittance of ITO/TB(MA) is similar to ITO glass, showing that the light absorbance of TB(MA) does not impact or interfere with the device's performance. Through atomic force microscopy (AFM), the root-mean-square (RMS) roughness obtained was 1.97 nm and 1.87 nm for TB(MA) and PEDOT: PSS films, respectively. These values show that both the layers make good enough HTMs to form suitable contact between the HTM/perovskite interface. The absorbance of ITO/HTM/$MAPbI_3$ is studied. Both films have similar absorbance spectra except for the regions below 550 nm.

From the X-Ray Diffraction (XRD) spectra, it is observed that the patterns for TB(MA) are stronger than PEDOT: PSS. This shows that the TB(MA) film has higher crystallinity in comparison to PEDOT: PSS. The diffraction peak of PbI_2 is around 12.5°, which cannot be seen in TB(MA) patterns. This suggests that there are little to no PbI_2 crystals in the TB(MA) film, with high purity. The scanning electronic microscopy (SEM) further validates the results by showing many patchy white grains in the PEDOT: PSS/$MAPbI_3$ film, whereas no such grains are noticed in the TB(MA)/$MAPbI_3$ film. The AFM measurements with the perovskite/HTM layer show an RMS roughness of 9.0 nm for TB(MA), which is much smoother than PEDOT: PSS (12.0 nm) due to the reduced number of PbI2 grains. The device (inverted PSC - IPSC) architecture used is ITO/HTM/MAPbI3/PCBM/BCP/Ag. As expected, the photovoltaic performance obtained from TB(MA)-PSC is above par, with J_{sc} = 23.45 mA/cm^2, V_{oc} = 1.08 V, FF = 78.0% and PCE = 19.76%. The obtained champion PCE is the highest reported PCE for an IPSC using CPE HTMs. The stabilized current density is 22.4 mA/cm2, and the maximum power point (MPP) is 19.0%. The integrated current densities obtained from the EQE measurements are 21.76 mA/cm^2 and 20.72 mA/cm^2 for TB(MA) and PEDOT: PSS devices, respectively, which coincides with the J-V values. The photovoltaic performance of TB(MA) and PEDOT:PSS-based devices are summarized using Table 2.

Table 2. Photovoltaic performance of IPSCs using PEDOT:PSS and TB(MA) HTMs

HTM	V_{oc} (V)	J_{sc} (mA/cm^2)	FF (%)	PCE (%)	R_s (Ω/cm^2)	R_{sh} (Ω/cm^2)
TB(MA)	1.08	22.93	75.90	18.82	35.69	9502.92
PEDOT:PSS	0.99	22.05	74.62	16.30	38.57	4433.34

The devices were placed in an inert atmosphere without encapsulation for 30 days. After 30 days, TB(MA) device retained 84% of its initial PCE, whereas its PEDOT: PSS lost 65% of its initial PCE. This shows the long-term stability of the device with steady control in under-regulated atmospheres. The PL measurements show that it increases under TB(MA) film. This indicates the lesser defects in the film and reduced irradiative recombination sites. Thus, the TB(MA) film can easily extract the photogenerated holes from the perovskite layer with greater efficiency. The TRPL spectra indicate that the fast decay constants are 27.74 ns and 5.26 ns. The slow decay constants are 67.30 ns and 20.69 ns for TB(MA) and PEDOT: PSS devices. The EIS spectra show a large R_{rec} for TB(MA) device, which depicts lower recombination probability due to fewer defects. The shunt resistances are 9502.92 Ω/cm^2 and 4433.34 Ω/cm^2 for TB(MA) and PEDOT: PSS devices. To calculate the density of trap states (DOS), thermal admittance spectroscopy (TAS) is used. The DOS values for shallow and deep traps for TB(MA) is 9.59 x 1015/cm^3 and 1.94 x 1017/cm^3 and for PEDOT:PSS is 2.43 x 1017/cm^3 and 5.09 x 1018/cm^3. It has been reported that shallow traps are at the grain boundaries. In contrast, deep traps are at the top or bottom of the perovskite layer. Since the PCBM layer passivates the top traps, the bottom traps are majorly affected by the passivation effect from the HTM/perovskite interface. The above values show that TB(MA) has lesser defects and is more compatible with IPSCs. The passivation by TB(MA) is capable because of the following reasons: a) the formation of coordinative bonds between amines and uncoordinated Pb^{2+} ions due to the lone pair of electrons in MA (Nitrogen atom) and b) filling the MA+ vacancies. The reduced traps at grain boundaries are due to the high crystalline films formed. This reduced trap number can help faster charge transport and thus contribute to a higher J_{sc} value. The lower charge recombination in the film increases V_{oc} despite both the films having similar work functions. This ultimately contributes to high PCE and FF. Most importantly, reduced defects improve the long-term stability of the device.

2.4 Perylenetetracarboxylic Dianhydride ETM

For n-i-p PSCs, the often-used ETMs are fullerenes and n-type materials. However, fullerenes possess certain disadvantages that make them unsuitable for practical applications. The costly nature, washed away by perovskite ink and high-processing temperatures (>200°C), makes it impossible to use flexible plastic substrates. It has been reported that the maximum processing temperature is 120°C to produce flexible PSCs on polyethylene terephthalate (PET) films. Although there are low-temperature fabrication methods for metal oxide deposition, the most appropriate step would be to discover appropriate ETMs with low-processing temperatures that can produce preferable photovoltaic performance without a high temperate annealing stage. Additionally, the organic ETM should be solution-processable, simple thermal evaporation, and compatible with roll-to-roll fabrication techniques. Perylenediimides (PDIs) are a new category of materials that have been studied due to their exceptional thermal stability and suitable energy alignment with the perovskite active layer [6-9]. PSCs with PDI-based ETM has delivered a PCE of nearly 11% with improved stability. Chemically modifying the PDI backbone improves the PCE to 19.8%. Similarly, Naphthalenediimide (NDI) derivatives like NDI-PhE have an optimized PCE of 20.5%. N-type conjugated polymers used as ETM had better surface coverage, reduced film roughness, and improved PCE of 17% for P(NDI2DTTTCN). Inorganic ETMs are typically used for inverted PSCs configurations. Using organic ETMs requires the material to satisfy high optical transparency and insolubility in the perovskite ink. Perylenetetracarboxylic dianhydride (PTCDA) is an example of an organic n-type semiconductor with superior charge transport properties because of π-π orbital overlap and reduced intermolecular distance in the crystal. Moreover, the electron mobility in PTCDA is high (0.08 cm^2/Vs). In this section, we will be looking into the works of Sergey Tsareva and co-workers using PTCDA in n-i-p PSCs. This configuration was also used for SnO2 coupled with PTCDA. PTCDA films can be deposited easily using low-temperature simple thermal evaporation methods using plastic substrates. Thus, these features make it a candidate for future uses [10]. PTCDA films have excellent surface coverage and wettability over the perovskite surface, as shown by the large wetting angle with water (23°) of the glass/PTCDA layer. The molecular solid π-

stacking makes it insoluble in organic solvents. This feature is possible for systems with planar π-conjugated formations without solubilizing the side chains. The device architecture used is ITO/PTCDA/$MAPbI_3$/PTA/MoO_3/Ag and ITO/SnO_2/PTCDA/$MAPbI_3$/PTA/MoO_3/Ag. PTCDA is used as a buffer layer in the second case to prevent SnO_2 from corroding the $MAPbI_3$ layer. Since the absorption of PTCDA film is near the visible region, it often gives rise to competitive absorption with the perovskite active layer. Hence, it is required to find the optimal thickness. The film should be thick enough to block holes but not too thin to provide recombination opportunities. The PTCDA thickness was gradually increased from 3 to 26 nm to find the optimal thickness. The transmittance spectra of PTCDA films on ITO/SnO_2 layers had two peaks at 480 and 560 nm. When the thickness of PTCDA is 26 nm, the transmitted light was below 15% for light at 500 nm. When the thickness is 3 nm, the transmitted light is 80% at 500 nm, which is 15% lesser than ITO/SnO_2 new film. Atomic Force Microscopy (AFM) measurements were studied to test the uniformity of the film. The 26 nm thick film had a smooth surface with minimal roughness representing the ITO profile. Figure 3 elaborates the molecular structure of the PTCDA molecule. Figure 4 shows the energy band alignment of all the device components.

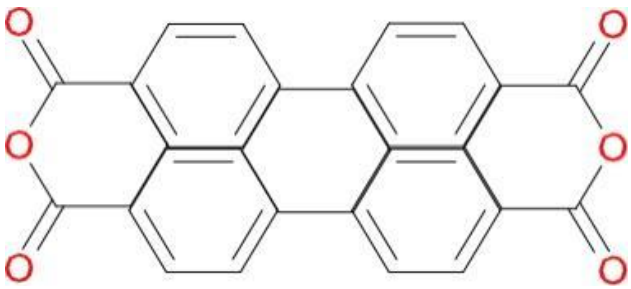

Figure 3. Chemical Molecular Structure of PTCDA

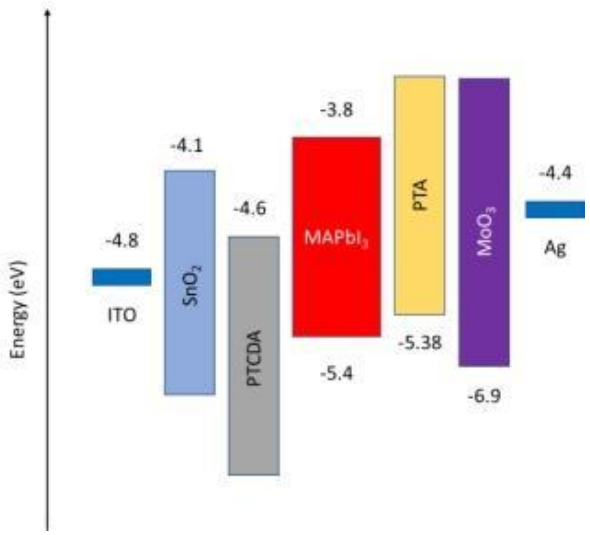

Figure 4. Energy Band alignment of PTCDA-device

PSCs using SnO_2 as the ETM had outputs of: Voc = 1007 ± 12 mV, J_{sc} = 20.6 ± 0.5 mA/cm², FF = 59 ± 3% and PCE = 12.4 ± 0.9%. The low values can be related to the non-passivating ability of SnO_2, which increases interfacial recombination and thus an energy barrier for electron transfer. The usage of 3 mm thin layer of PTCDA significantly improves the output of the device: V_{oc} = 957 ± 24 mV, J_{sc} = 21.3 ± 0.4 mA/cm², FF = 69 ± 4% and PCE = 14.1 ± 1.2%. It is important to note that despite the optical losses due to the PTCDA film, the passivating effect reduces interfacial recombination greatly, which improves the performance of the device when compared to SnO_2. However, the lower value of V_{oc} can be attributed to the slight misalignment in energy bands with the perovskite layer. Increasing the PTCDA film thickness to 26 mm, there was no improvement in FF, V_{oc} and the J_{sc} decreased to 19 mA/cm² due to optical losses. Similarly, a device that used just a plain PTCDA film as the ETM showed the best performance for 3 mm thickness. The highest PCE obtained was 14.3% for PTCDA-based devices, higher than SnO_2 based devices. These results show that using PTCDA will improve the FF and reduce the recombination of charge carriers at the perovskite/ETM interface. The misalignment in energy levels with the perovskite layer can be altered by chemical modification, the addition of dopants, or sidechain engineering. This way, we can obtain higher PCE.

ITO/ETM/$MAPbI_3$/PTA/MoO_3/Al configuration was adopted to test operational stability. The device was aged at 60 ± 2 °C, and 91±5 mW/cm² of white LED light in an inert atmosphere. The MoO_3/Al architecture is used in this case because it has been reported that MoO_3 forms a barrier layer for metal diffusion by forming a thin alumina layer. On testing both the cells, they degraded rapidly under elevated temperatures and light intensity. However, in comparing both films, the PTCDA ETM showed better stability. Studying the variation of FF and V_{oc}, the PTCDA addition improved the diode ideality factor from 1.48 to 1.44 as it reduced the interfacial recombination. On analyzing the FF and light intensity variation, the FF of devices with SnO_2/PTCDA and SnO_2 ETMs increase when light intensity is decreased. This is due to the increase in charge recombination and its impact on FF. Whereas for the plain PTCDA film, the FF and V_{oc} decreased when light intensity was reduced. This can be attributed to the impact of R_{sh} where a thin film of PTCDA has insufficient hole blocking ability.

2.5 Fluorinated Fulleropyrrolidine as ETM

For direct PSCs, the conventional ETMs are $PC_{61}BM$ and C_{60}. The solution processibility and suitable energy band alignment with the perovskite and hydrophobic nature are advantages that make these materials favorable for ETM. Fullerene acceptors like indene-C_{60} and C_{70} bisadduct have been used previously as an ETM but have yielded poor PCE levels. This can be attributed to the higher LUMO levels of these materials concerning $PC_{61}BM$. C_{60} and $PC_{61}BM$ have other drawbacks such as low photovoltaic performance, lower electrical conductivity, and inferior hydrophobic properties. Fluorinated compounds have higher thermal and moisture resistance, whereas even fluoropolymers developed have enhanced stability. However, fluorine-derived compounds cannot be used directly as an ETM due to their low carrier mobility. Hence, fluoro-substituted fullerenes can

be considered a viable option where the developed devices can have improved stability and long-term operational ability [11-15]. It is important to note that fluoro-substituted fullerenes have never been used previously for inorganic PSCs. In this section, Quan Yuan and coworkers fabricated two fluoro-substituted fullerene compounds termed FP-i and FP-ii used in an organic-inorganic PSC with $MAPbI_{3-x}Cl_x$ and inorganic PSC with $CsPbI_2Br$. The FP-i compounds here is 2-(perfluorophenyl)-5-phenyl-C_{60}-fulleropyrrolidine and FP-ii is 2,5-bis-(perfluorophenyl)-C_{60}-fulleropyrrolidine.

The architecture used in organic-inorganic device is ITO/PEDOT:PSS/$MAPbI_{3-x}Cl_x$/HTM/BCP/Ag and for the inorganic device is ITO/NiO_x/$CsPbI_2Br$/HTM/Bephen/Ag [16]. The excellent solubility of FP-i and FP-ii in o-DCB enables low-temperature solution processing. From the UV-Vis spectroscopy, the absorption spectra show that both fullerene derivatives have a peak at 420-430 nm. With and without the ETM, the perovskite shows a similar absorption spectrum. This implies that the ETM addition does not influence the absorption characteristics of the perovskite layer. Through the cyclic voltammetry tests (CV), the electrochemical properties of the ETMs were measured. Both FP-i and FP-ii showed two reversible reduction waves in the 0 ~1.6 V range. The reduction potentials were calculated with Ered1/2 = 1.20 V for PC61BM, and Ered1/2 of FP-i and FP-ii are shifted by 10-20 mV. This can be attributed to the electron-withdrawing effect of the perfluorophenyl substitution. The calculated LUMO levels of FP-i and FP-ii are -3.94 eV and -3.95 eV, which is deeper than the LUMO level of PC61BM (-3.93 eV). Hence, we can conclude that based on the arrangement of LUMO levels. The trend is FP-ii < FP-i < PC61BM.

The AFM, SEM, and water contact angle measurements are studied. In the case of PVK/PC61BM, the film developed had a uniform structure with a root-means-square (RMS) roughness of 5.67 nm. The RMS roughness obtained in the fluoro-substituted fullerene cases is 6.48 and 6.05 nm for FP-i and FP-ii, respectively. Although the values might seem higher, the deposition of a thin layer of BCP reduces the roughness. It produces a more uniform film to facilitate smoother interfacial contact between the stacks in the device. The water contact angles obtained were 97° and 105° for FP-i and FP-ii. This can be justified by the hydrophobic nature of fluorine substituted products which can provide the device with greater stability against moisture and extrinsic factors. The optimal thickness of FP-i and FP-ii films was 30 nm. From the device layout, it is visible that the LUMO levels of the fluoro-substituted fullerene match well with the CBM of the perovskite. Thirty devices of each ETM were fabricated, and the best performances were recorded. The output PCE for FP-i and FP-ii-based devices was 13.6% and 14.2%, respectively, higher than the PC61BM-based devices (12.7%). However, the FP-i and FP-ii devices had lower V_{oc} and hysteresis when compared to PC61BM. This can be related to the mismatch in deeper LUMO levels of fluoro-substituted fullerenes, producing more energy loss in interfacial charge transfer. Moreover, the increased energy losses can even accumulate more charges at the PVK/ETM interface. However, the J_{sc} and FF values obtained were higher in the case of fluoro-substituted fullerenes. The EQE spectra are studied to evaluate the increase in J_{sc} and FF. FP-i and FP-ii devices showed higher EQE values in the absorption range of 350-750 nm compared to PC61BM. The integrated J_{sc} values obtained are 19.0, 20.1, and 20.5 mA/cm^2 for PC61BM, FP-i, and FP-ii-based devices. These results were validated with the obtained J-V outputs with a difference of 8%.

The steady-state power outputs (SPOs) at 0.81 V were 13.5% and 14.2% with photocurrents of 16.7 and 17.6 mA/cm2. These obtained values are higher than the PC61BM device, with an SPO value of 12.6% and a photocurrent value of 15.6 mA/cm^2. On conducting humidity-based stability tests at 40-50% RH for 70 hours, FP-i and FP-ii devices showed better stability characteristics. PC61BM retained only 40% of its initial PCE value. In contrast, FP-i and FP-ii-based devices retained 70-85% of their initial PCE value. The PL emission of the perovskite configuration is relatively strong at 775 nm, and this PL emission is quenched by introducing various ETMs. This result indicates that similar to PC61BM, FP-i and FP-ii have excellent charge extraction capabilities and dynamic properties. The TRPL spectra reveal that the average decay lifetime is 16.8, 15.3, and 16.8 ns for FP-i, FP-ii, and PC61BM, respectively. The time constant values obtained here depict the films' superior charge extraction and collection properties. The space-charge-limited current (SCLC) model measurements were taken to study the trap density in perovskite/ETM configurations.

The N_{trap} values were found to be 4.25 x 1016 cm^{-3}, 4.17 x 1016 cm^{-3} and 7.18 x 1016 cm^{-3} for FP-i, FP-ii and PC61BM devices respectively. These results show the passivation effect that FP-i and FP-ii films possess compared to PC61BM. The variation of V_{oc} and light intensity is studied to validate the passivation effect. The FP-i and FP-ii devices had a weaker dependency on V_{oc} with a lesser slope of 1.10KBT/q and 1.13KBT/q, respectively. PC61BM showed a more significant dependence on V_{oc} with a value of 1.24KBT/q. These results show that FP-i and FP-ii-based devices have lesser non-radiative and interfacial recombination of charge carriers. The FT-IR spectra show the shift of N-H---F vibration modes due to hydrogen bonds to a lower wave number. A similar phenomenon can be observed for NaF-based PSCs. Figure 5 depicts the hybrid and inorganic PSC device architectures using different fluorinated molecules. Figure 6 shows the energy band diagram of the PSC device materials in a relative manner to FP-i and FP-ii.

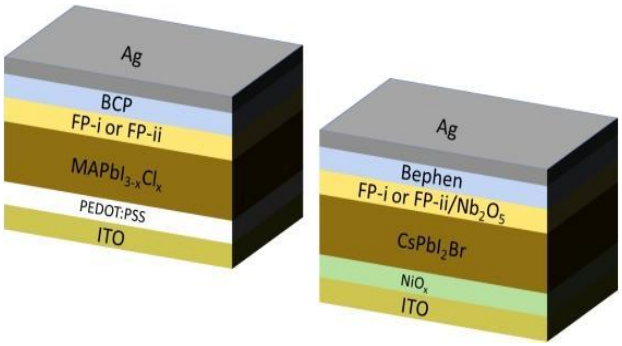

Figure 5. Hybrid and Inorganic PSC devices using FP-i and FP-ii HTMs

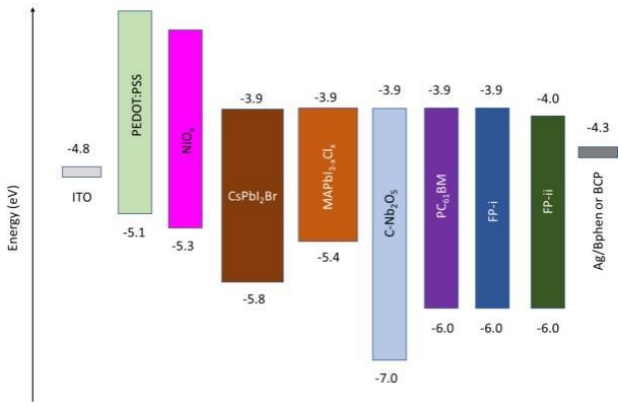

Figure 6. Energy Band alignment of all materials used in both PSC devices

It was using FP-i and FP-ii in inorganic PSCs containing $CsPbI_2Br$. In this case, the energy levels were aligned well with the CBM of the perovskite active layer. Similarly, the FP-i and FP-ii-based devices had lower V_{oc} values but higher J_{sc} and FF values. The lower V_{oc} values can be related to the deeper LUMO level of fluoro-substituted fullerene. However, the higher values of J_{sc} and FF are due to the large conductivity values. The PCE values obtained were comparable to the PC61BM and ZnO/C_{60}-based devices. The EQE measurements were taken, and the obtained values were confirmed with the J-V tests with a nearly 5% difference. The SPO value was found to be 10% for 110 seconds. The V_{oc} vs light intensity dependency was studied as 2.29KBT/q, 1.93KBT/q, and 1.74KBT/q for PC61BM, FP-i, and FP-ii-based PSCs. The stability tests for thermal aging at 80oC after 430 hours showed that FP-i and FP-ii devices retained 85-95% of their initial PCE. This indicated an enhanced thermal stability property compared to the champion performance of ZnO/C60 ETM.

2.6 TPD as HTM in PSCs

In inverted PSCs (IPSCs), the HTM is one of the most crucial layers in the device. It should affect the crystallization rate, have higher hole extraction efficiency, and should not corrode the electrode. PEDOT: PSS has a low work function of 4.9-5.2 eV, which is responsible for high energy losses, consequently reducing the V_{oc} values. Inorganic HTMs such as NiO_x, V2O5, CuO, CuSCN, and CuI have also been used as an alternative to current organic HTMs because of their good hole mobility, thermal stability, and low material cost. However, these materials' high-temperature processing conditions (>500°C) make it harder to commercialize these PV technologies. These abrasive conditions make it difficult to model PSCs on flexible plastic substrates. Alternatives to PEDOT: PSS have been non-wetting polymers that have produced devices with excellent performance, suitable energy band alignment, appropriate preparation methods, and complimenting other layers in the PSC stack. Xu et al showed that poly(N,N'-bis(4-butylphenyl)-N,N'-bis(phenyl)benzidine) (poly-TPD) as a HTM in IPSCs yielded a PCE of 18.1% [17]. Similarly, Liu et Al developed a HTM using poly(bis(4-phenyl) (2,4,6-trimethylphenyl)amine) (PTAA) to attain a PCE of 20.7% [18]. Yang et Al fabricated a thin film of poly[(9,9-dioctylfluorenyl-2,7-diyl)-co-(4,40-(N-(4-sec-butylphenyl) diphenylamine)] (TFB) to achieve a PCE of 20% [19]. However, polymers such as PTAA, poly-TPD, TFB, etc., are costly, making it unfavorable to use these materials on a large scale. Thus, the next step in the research is to develop a suitable HTM that can be fabricated at low temperatures, is efficient, and is low priced. In this section, Zijun Wang and co-workers developed N,N'-bis(3-methylphenyl)-N,N'-bis(phenyl) benzidine (TPD), which is an organic, small, hydrophobic, cheap, and low-temperature processable material that can be used a potential HTM [20]. The transmission spectra of TPD show negligible absorption in the visible region. Thus we can conclude that there will be no notable optical losses for greater photovoltaic performance. The TPD film showed greater surface coverage after thermal annealing through optical microscopy measurements. The energy band alignment allows TPD to extract more holes than PEDOT: PSS. The HOMO level of TPD is -5.4 eV, whereas that of PEDOT: PSS is 5.2 eV. This enables lesser energy losses, greater hole extraction efficiency, and higher V_{oc} and device performance values. The concentrations of the TPD precursor solution were varied to find the optimum film thickness. It is taken to verify each governing photovoltaic performance. At TPD concentration = 4 mg/mL, the highest performance is obtained with a PCE = 19.77%, Jsc = 22.95 mA/cm^2, V_{oc} = 1.075 V, FF = 80.12% and film thickness of nearly 35 nm. On further increasing the concentration of the TPD HTM, the performance begins to decrease. This can be attributed to the increasing resistance as film thickness increases, increasing the series resistance of the entire device. The average PCE reported for 0.5, 2, 4, 6, 8 and 10 mg/mL concentration of TPD is 16.61%, 17.61%, 18.32%, 17.05%, 16.51% and 14.99% respectively. These average values for 16 devices confirm that TPD-based PSCs have good reproducibility. In other cases, the optimal concentration of 4 mg/mL will be used as an HTM.

Due to the formation of hydrogen bonds, the passivation of fluoro-substituted fullerene is superior and effective. Using the Ag/ETM/Ag configuration, the conductivities of the ETMs are studied. The relation used to calculate the same is I = σoAL-1V. The calculated σo values are 14.12, 16.05, and 16.96 μS/cm for PC61BM, FP-i, and FP-ii films, respectively. The calculated lateral conductivities are 7.5, 8.1, and 6.2 S/cm for PC61BM, FP-i, and FP-ii films. The higher conductivity values for fluoro-substituted fullerene validate why these devices have higher J_{sc} and FF values. Figure 7 shows the energy band alignment of the device materials, which accounts for suitable charge transfer and separation.

Using PEDOT:PSS as a HTM for IPSCs the obtained output values are, J_{sc} = 21.18 mA/cm^2, V_{oc} = 0.90 V, PCE = 14.83% and FF = 77.61%. When TPD replaced PEDOT: PSS, the device performance increased considerably with a substantial increase in V_{oc} and J_{sc} values. TPD-based devices showed negligible hysteresis effects when taking forward and reverse scanning measurements. The EQE measurements show that TPD has a higher efficiency value of >80%, whereas PEDOT: PSS has an efficiency value of >70% in the 400 to 750 nm region. The integrated J_{sc} values are 20.09 and 22.78 mA/cm^2 for PEDOT: PSS and TPD-based devices. The devices were further tested under maximum power point (MPP) conditions at AM 1.5G illumination for 250 seconds. PEDOT: PSS had a V_{max} = 0.80 V, and TPD had a V_{max} = 0.93 V.

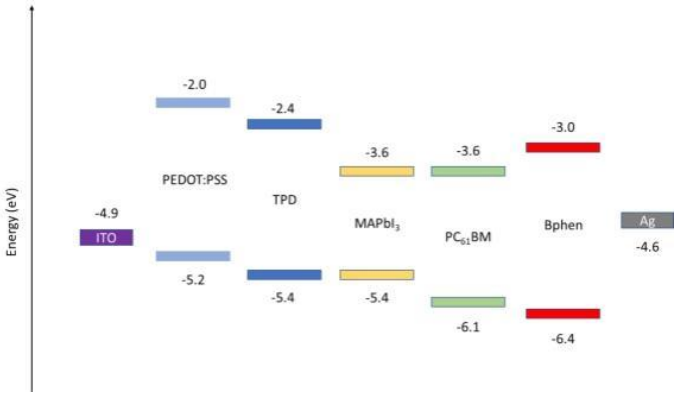

Figure 7. Energy Band alignment of TPD

To evaluate the film morphology and its characteristics, the SEM measurements were studied. The SEM analysis shows no pinhole formations for both PEDOT: PSS and TPD films. The TPD film produced perovskites with larger grain size (~300 nm) when compared to PEDOT: PSS (~200 nm). It is important to note that the larger the grain size, the lower the grain boundary density. This reduces the grain boundary defects and consequently improves the device performance. The water contact angle (WCA) measurements show a value of 25° for PEDOT: PSS and 75° for TPD. This increase in water contact angle for TPD can be attributed to the larger grain size, which gives it a hydrophobic property. When the same volume of perovskite precursor solution (10 µL) was dropped onto each of the HTMs, PEDOT: PSS film spread the solution rapidly across its surface, but a similar phenomenon was not observed in TPD, which shows its high hydrophobic property. This water repelling property is extremely beneficial for the long-term stability of the device. It increases the moisture resistance of the device. The long-term stability of the devices was tested by storing them in a glovebox under ambient conditions for one month. After one month of storage, the PCE values were tested. It was noticed that PEDOT: PSS-based device could retain only 62.3% of its initial PCE value, whereas TPD-based device could retain 84.1% of its initial PCE value. On studying the XRD patterns, the diffraction patterns show that PEDOT: PSS has an average crystal size of 59.6 nm, and TPD has an average crystal size of 77.2 nm. These results indicate that TPD usage as an HTM in IPSCs can even support perovskite crystal growth. The obtained XRD results are consistent with the previously studied SEM results. The UV-Vis absorption spectra show that both films have a vital absorption feature in the 450-800 nm range. On studying the PL and TRPL measurements, both films showed a characteristic peak at 770 nm, a feature of the MAPbI3 perovskite. However, TPD had a weaker PL emission, indicating the perovskite layer's efficient hole extraction and collection ability. The decay constants from TRPL can be mathematically modeled. The average lifetime (Tave) values obtained 35.53 ns and 19.01 ns for PEDOT: PSS/PVK and TPD/PVK interface.

The lower the lifetime, the greater the efficiency of charge extraction from the perovskite layer and thus higher device performance.

2.7 Tetrathiafulvalene Derivative as an HTM

Currently, for various PSCs, several small molecules and polymeric HTMs have been used. These standard HTMs have been used extensively to produce excellent PCE values and stability devices. However, the lower value of charge mobility requires the addition of additional dopants. Although dopants are highly beneficial in altering the material's properties, these extrinsic dopants impact the long-term stability of the device, found to be corrosive, hygroscopic, and expensive. There have been non-hygroscopic dopants developed, but the effect these materials have on the long-term stability of the device is considered detrimental [21, 22]. Due to their superior hole-transporting properties, organosulphur TTF compounds and their derivatives have been used as HTMs. The significant electron-donating properties, charge transfer complexes, electroactive metal complexes, and radical cation salts make TTF and its derivatives useful HTMs. Haseeb Ashraf Malik and co-workers fabricated a TTF derivative with four methoxy (O-Me) groups as a successful HTM that paves the way for dopant-free HTMs in PSCs. The usage of methoxy groups in PSCs as an HTM has previously shown its superior device performance [23]. The device architecture used in this section is FTO/c-TiO_2/m-TiO_2/perovskite/TTF-derivative/Au. The various concentrations of the HTM precursor solution were taken, deposited, and studied the performance. It was found that a concentration of 20 mg/mL was the optimal concentration with an active device area of 0.09 cm^2. To conduct a comparative analysis of the device performance, the HTM was also replaced with pristine spiro-OMeTAD. The thermal and long-term stability of the device was evaluated using TGA analysis at elevated temperatures. It was found that only 5% of weight loss occurred at temperatures of 293°C. This value was then compared with spiro-OMeTAD-based HTM, showing thermal stability up to 400°C. This value can be attributed to the molecular arrangement within the molecule. Studies have shown that molecular size, chain length, and structural dimension impact thermal stability significantly. Molecules with multiply branched structures and bulky substitutes often show greater thermal stability values. The large and branched structure of spiro-OMeTAD improves its thermal stability compared to the TTF derivative. Moreover, the significant difference in molecular weight between spiro-OMeTAD (1225.43 g/mol) and TTF (757.10 g/mol) is another added reason for its better thermal stability. The UV-Vis absorption spectra show that the absorption range for TTF is between 280 and 450 nm, with an absorption peak between 290 and 300 nm and a secondary peak around 400 nm. The peaks can be attributed to the n-π* and π-π* absorption bands. TTF shows a maximum emission peak at 437 nm. The intersection between the emission and absorption spectra can be used to calculate the bandgap of the fabricated TTF molecule, which was found to be 3.08 eV. An ideal HTM should be positioned so that the VBM of the perovskite is more harmful when compared to the HOMO of the HTM. This ensures efficient transport of holes and fewer energy losses. The LUMO of the HTM should be positioned above the CBM of the perovskite. This ensures that

electrons are blocked, and no electrons flow to the cathode. The CV analysis was conducted on TTF to study the energy band alignment. The HOMO level is directly related to the first oxidation potential (E_{ox}), which equals 0.65 V for an Ag/AgCl electrode. The HOMO level was recalibrated using mathematical modeling using a Normal Hydrogen Electrode (NHE). The value of TTF as an HTM in a vacuum was found to be EHOMO = -(E_{ox} + 4.50) eV, which equals -5.35 eV. This value validates the favorable energy band alignment with the perovskite layer with efficient charge transporting properties. Similarly, ultraviolet photoelectron spectroscopy (UPS) measurements were taken to study the energy level alignment further. The HOMO level in a vacuum was calculated using the mathematical formula $\phi = 21.22 - (E_{cutoff} - E_i)$, which equals -5.30 eV. This value validates the answer obtained using CV measurements. The LUMO level was calculated using the relationship $E_{LUMO} = E_{HOMO} - E_{0\text{-}0}$, which equals -2.27 eV. Once again, the obtained values confirmed that the HOMO and LUMO levels of TTF matched well with the CB and VB levels of the perovskite layer. The SEM analysis was used to study the film morphology. The device structure showed a film with superior uniformity, large grain size, no pinhole formation, and excellent surface coverage. The cross-sectional SEM analysis revealed the various layers of the PSCs and the compatibility of various stacks within the device.

The device was tested under 100 mW/cm^2 AM 1.5G controlled radiation. Various concentrations of the TTF precursor solution were deposited, and the corresponding performance was studied. It was found that a concentration of 20 mg/ml showed the best performance with a PCE = 15.66%, J_{sc} = 20.14 mA/cm^2, V_{oc} = 1.04 V and FF = 0.74. The performance for 15, 17, 19, and 21 mg/ml was recorded. The general pattern that this followed was that there was a gradual increase in performance on increasing the concentration. However, the performance decreased significantly by increasing the concentration above 20 mg/ml. These performance values were compared with pristine spiro-OMeTAD. The values obtained were extremely inferior with a J_{sc} = 18.62 mA/cm^2, V_{oc} = 0.98 V, PCE = 12.79% and a FF = 0.69. Similarly, an HTM-free PSC was developed, and the highest PCE reported from it was 8.5%. The IPCE spectrum shows that the integrated J_{sc} values of TTF, spiro-OMeTAD, and HTM-free PSC are 19.41 mA/cm^2, 17.49 mA/cm^2, and 13.89 mA/cm^2, respectively. The integrated Jsc values were in complete agreement with the Jsc value from the J-V tests. The PL measurements were conducted for the perovskite/HTM and perovskite architecture. There is a notable emission peak at 762 nm related to the perovskite layer. There is a considerable amount of quenching effect that is seen in the perovskite/HTM bi-layer configuration. This indicates the efficient hole transfer capabilities and charge dynamics within the layer. The perovskite/TTF is 64% more quenched in comparison. This shows the smooth transfer of holes with minimal energy losses and favorable hole transfer. The fitted TRPL shows that decay time Tperovskite (39.91 ns) < THTM (68.41 ns) implies the superior hole extraction ability of TTF from the perovskite/HTM interface. The hole mobility of both materials was studied using space charge limited current analysis. The carrier mobility was found using the equation:-

$$J = (9\mu\varepsilon_0\varepsilon_r V^2)/(8L^3)$$ - Mott Gurney's equation

The resulting hole mobility was calculated to be 4.804 x 10^{-5} cm^{2}V/s and 2.36 x 10^{-5} cm^{2}V/s for TTF and spiro-OMeTAD, respectively. The stability of the devices was tested under ambient conditions where they were stored under an RH ≥ 70%. The PCE of the devices was studied after every 45 days. It was found that TTF HTM could retain 84% of its initial PCE values. In contrast, spiro-OMeTAD HTM could retain only 56% of its initial PCE after 45 days of aging. To further study the stability factors in the TTF-based device, the device was exposed to the same conditions for 45 days with periodic investigations every 15 days, without any encapsulation. The study showed that the upper surface of the PSC had minimal degradation for extrinsic factors. However, the perovskite active layer was still intact. There was no prominent discoloration (yellow), and only the layer exposed most to the atmosphere showed few signs of degradation. The water contact angle measurements show 91.02^o and 79.6^o TTF and spiro-OMeTAD, respectively. This high-water contact angle of TTF shows its hydrophobic ability and moisture stability to further increase its long-term performance.

2.8 Dopant-free Organic HTMs

Xu et al. fabricated 2 HTMs using indacenodithiophene (IDT) units with long alkyl substituent chains. The co-planar geometry of IDT allows high intermolecular interaction and consequently higher hole mobility. Sun and Johansson et al. developed a dopant-free HTM that uses ionic units with greater higher hole mobility and conductivity, thus higher PCE than spiro-OMeTAD-based devices [24]. Jen and Chen et al. fabricated a new HTM that uses a C3h truxene core known as Trux-OMeTAD that produced a PCE of 18.6% with negligible hysteresis. The molecule's geometry allowed suitable hole mobility and appropriate energy band alignment with the subsequent layers in the device. HTMs using spiro[fluorine 9, 9'-xanthene] (SFX) have been developed. Its sp3-hybridized carbon between two perpendicular π planes forms a 3D structure that ensures reduced charge recombination, electronic coupling, and improved charge transportability [25]. The procurement cost of SFX is nearly 30 times lesser than spiro-bi[fluorine] (SBF), with a synthesis yield of > 90% when phenol and 9-fluorenone are used as the raw materials. Hence, the next target is to develop dopant-free HTMs and have appropriate hole mobility and conductivity values. In this section, Linqin Wang and co-workers developed two dopant-free HTMs such as N2',N2',N7',N7'-

tetrakis(4-methoxyphenyl)spiro[dibenzo[c,h] xanthene-7,9'-fluorene]-2',7'-diamine (X61) and N2',N2',N5,N5,N7',N7',N9,N9-octakis(4-methoxyphenyl)spiro [dibenzo[c,h]xanthene-7,9'-fluorene]-2',5,7',9-tetraamine (X62), with spiro[dibenzo[c,h]xanthene-7,9'-fluorene] (SDBXF). The SDBXF skeleton has a spiro-core that adds to more π-conjugation systems than the SFX unit. The added naphthalene group can further increase conjugation and improve π-π stacking, improving charge transport [26]. Figure 8 shows a clear depiction of the energy band diagram of all the materials in the device including the synthesized molecules and the device architecture of the fabricated device.

The UV-Vis absorption spectra show that X61 and X62 films have similar absorption peaks at nearly 382 nm. The

region for visible light (~430 nm) has a very narrow region. This indicates that X61 and X62 have lower optical losses and will not interfere with the absorption ability of the perovskite layer. The emission peaks of X61 and X62 are found to be at 432 nm and 483 nm, respectively, where we conclude that dimethoxydiphenylamine units do not influence the absorption characteristics but have a significant say in the emission properties.

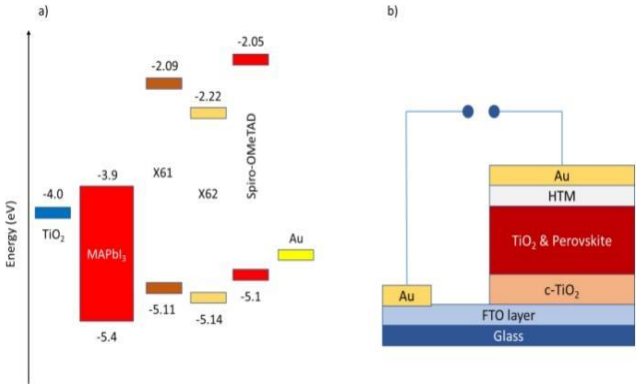

Figure 8. a) Energy Band diagram of X61 and X62, b) PSC device architecture

The intersection of the absorption and emission data can be used to calculate the material's bandgap. It is found that the HOMO level of X61 and X62 is -5.11 and -5.14 eV, respectively. This value is close to spiro-OMeTAD (-5.10 eV). The similarity in values shows that X61 and X62 can efficiently transport holes right from the perovskite/HTM interface to the Au counter electrode. Similarly, the LUMO level is calculated to be -2.09 and -2.22 eV for X61 and X62, respectively, which is in suitable alignment with the CB of the perovskite. This allows the efficient blocking of electrons and prevents charge recombination to a great extent.

Density Functional Theory (DFT) measurements are taken to study the molecular orbitals' energy levels and electron distribution. The HOMO levels are delocalized in the bottom fluorene and dimethoxydiphenylamine units. The LUMO levels are delocalized in dibenzo-xanthene units. This difference between the HOMO and LUMO levels is suitable for efficient hole transfer properties. The space charge limited current (SCLC) model evaluates the hole mobility and conductivity values. The hole conductivity is 5.14 x 10-6 S/cm, 3.98 x 10-6 S/cm and 4.56 x 10-6 S/cm for X62, X61 and spiro-OMeTAD, respectively. The larger conjugation system and structural extension in X62 results in greater π-π stacking, which can be one of the reasons for higher hole conductivity. The hole mobility is calculated to be 7.95 x 10-5, 3.91 x 10^{-5} and 6.06 x 10^{-5} cm^2/Vs for X62, X61, and spiro-OMeTAD. The device's architecture used is FTO/c-TiO_2/m-TiO_2/mixed-perovskite/HTM/Au. The optimal concentration for the HTMs is 18 mg/mL. The scanning electron microscopy (SEM) indicates that the HTM has excellent surface coverage when the concentration is higher than 15 mg/mL. The X62 film forms a better film with reduced charge recombination, which can be validated by the EIS results (high R_{rec} value). The output values for the X62-based device is found to be Jsc = 22.4 mA/cm^2, V_{oc} = 1.01 V, FF = 70.4% and PCE = 15.9%. The X61-based device shows an average PCE of 8%, J_{sc} = 18.6 mA/cm^2, V_{oc} = 0.97 V and FF = 44.1%. These values can be compared to the spiro-OMeTAD-based device with a J_{sc} = 19.9 mA/cm^2, V_{oc} = 1.04 V, FF = 52.6% and PCE = 10.8%. The IPCE spectra and the calculated integrated J_{sc} values show that the X62-based PSC is higher than X61 and spiro-OMeTAD-based PSC. The higher value of Jsc for X62 can be attributed to its efficient hole collection properties. The hole collection properties depend mainly on the hole conductivity and mobility values, which are superior in X62. The lower hole mobility and conductivity of X61 and spiro-OMeTAD increase the device's series resistance (Rs). This can be validated with the EIS results. The higher Rs value reduces the FF and thus the PCE of the device. The lower values of Voc for X61 and X62 can be due to the recombination losses in these materials. The devices were placed in ambient conditions under 50% RH at room temperature to study the device stability. On investigating after ten days, the devices retained 81%, 49%, and 80% of their initial PCE value for spiro-OMeTAD, X61, and X62-based PSC, respectively. The PL and TRPL measurements are taken to study the charge transfer dynamics and its mobility within the device. The perovskite film shows a half-time constant of 85 ns. When this film is coupled with X61, the half-time constant is reduced to 7.6 ns and 7.1 ns for X62. The reduced time constant value indicates the materials' tight hole extraction and collection properties, which justifies the high J_{sc} values. The X61 and X62 films are grown by the liquid diffusion method from organic solvents to study the impact of charge transport in the HTM. Using single-crystal X-ray diffraction (SCXRD), the crystal structure of X61 and X62 is studied. The dihedral angle between dibenzo[c,h]xanthene (DBX) and fluorene units are 89.6° and 89.2° for X61 and X62, respectively. The dihedral angle for spiro-OMeTAD is 89.9°. From the dihedral angles, it is evident that there are weak molecular interactions and molecular stacking useful for amorphous solid formation. The angles between the naphthalene units next to the non-aromatic central ring are 2.5° and 15.3° for X61 and X62, respectively. This again indicates the weak π-π interaction between DBX units, limiting dense molecular packing. For X61, the shortest contact distance between DBX and dimethoxyphenylamine unit is 3.216 A°. The interaction distance for the CH/π and O-H bonds is 2.808 and 2.659 A_o. Similarly, for X62, the CH/π, O-H, and C-O bonds and shortest contact distance are 2.882 A°, 2.567 A°, 3.112 A°, and 3.313 Ao. The presence of several short contacts in the X62 molecule ensures effective charge transport to result in better performance. Incorporating substituents such as dibenzo[c,h]xanthene skeleton can further improve the charge transport properties and facilitate the PCE of the device.

2.9 Metal Oxide/Organic Double HTM

The cause of hysteresis in PSCs is not yet known. However, processes like charge dynamics, ion migration and displacement, capacitance effects, and ferroelectric effects are considered the significant causes of hysteresis. The presence of halide ions in the perovskite active layer and their associated vacancies decide PSC performance. The mobility of these ions when scanning in different directions is done. There might be an accumulation of the ions at the interface for a brief period. This mobility of ions is influenced by the internal electric field present in the device. When ions are

collected at the interface, the strength of the internal electric field is masked by these ions and consequently impacting device performance as there is no efficient charge collection which eventually leads to hysteresis [27, 28]. Strategies like altering the charge transport layers through passivation effects and modifying the perovskite/charge transport material interface are a few techniques used previously to minimize device hysteresis. Huang et al. showed that depositing fullerenes on perovskite films can reduce trap density due to its inherent passivation ability, which nearly removed hysteresis. Park and co-workers showed that regulating the iodide-caused vacancies by placing the Frenkel defects of iodide ions into the O-gap position or doping with Kalium Iodidum. However, incorporating such methods requires immense skill, expertise, and fabrication costs. In this section, Fan Wu and co-workers have developed an inorganic/organic double HTM-based device using NiO_x/PEDOT: PSS to produce a device with reduced hysteresis [29]. The SEM measurements of NiO_x, PEDOT: PSS, and NiO_x/PEDOT: PSS are studied on an FTO glass substrate. The average thickness of the HTM is 30, 22, and 50 nm for the NiO_x, PEDOT: PSS, and NiO_x/PEDOT: PSS layers, respectively. The perovskite grain sizes are similar in all the films, where they showed uniform surface coverage across the perovskite along with the absorbance values that validate the crystal size. Device N, P, and N+P use NiO_x, PEDOT: PSS, and NiO_x/PEDOT: PSS, respectively, as their corresponding HTMs. The J-V plots were analyzed under AM 1.5G illumination and forward and reverse scans to calculate the hysteresis index. The hysteresis index (HI) can be calculated using the formula:

$$HI = ((PCE_{reverse} - PCE_{forward})/PCE_{reverse})$$

Device N showed a HI value = 0.142, the highest value, followed by Device P with an HI of 0.093. Lastly, Device N+P showed a HI of 0.020, which shows a reduced hysteresis value. The poor interfacial contact between NiO_x/perovskite layer results in reduced crystallinity of the perovskite, which inhibits charge transport and increases the hysteresis effect. NiO_x that is solution-treated induces Ni^{3+} vacancies along with prevailing defects. The PSS group in PEDOT: PSS is slightly acidic, having a PSS^- group that couples with Ni3+ defects to form an interfacial dipole layer through strong coulombic interactions. This created dipole points in the direction of PEDOT: PSS. Hence, when PEDOT: PSS and NiO_x come in contact, the above-mentioned dipole moment is created along with hydrogen bonds between H in PEDOT: PSS and O in NiO_x. The calculated dipole moment, μ using the formula $\mu = Q \times l$ where $Q = 2.036 \times 10^{-20}$ C and l = 4.877 A^o. The calculated μ is 9.929×10^{-30} cm, equal to 2.977 Debye, pointing from PEDOT: PSS to NiO_x with electrons flowing from NiO_x to PEDOT: PSS. Usually, when a dipole exists in a PSC, a vacuum level offset is created, which shifts the voltage during J-V dark operation. A similar process can be observed between the P3HT/metal electrode interface. This dipole moment favors hole extraction, clearly noticed through the reduced HI value. The EIS analysis was conducted to study the interfacial charge transport dynamics with different HTMs. The semi-circle in the high-frequency range is associated with the charge transfer resistance at ETM and HTM/perovskite interface. The second semi-circle at the low-frequency range is associated with the charge transfer between the ETM and HTM/perovskite interface.

The charge transfer resistance (R_{tr}) is 614, 308, and 121Ω for Device N, P, and N+P, respectively. It is evident that the greater thickness of the double HTM of NiO_x/PEDOT: PSS will give rise to higher series resistance (Rs). The R_{rec} values obtained for Device N+P (3.69 x 103 Ω) were comparatively higher, indicating the reduced charge recombination rates and the favorable dipole moment, which facilitates suitable charge extraction and collection. The charge dynamics can be further studied using intensity-modulated photocurrent spectroscopy (IMPSC). The semicircle in the high-frequency region is governed by series resistance (R_s) and geometric capacitance (C_{geo}). The semicircle in the low-frequency region concerns the charge relaxation process governed by the charge transport and recombination process.

The k_{trans} values for all the HTMs are calculated, representing the charge transport rate and k_{rec} representing the charge recombination rate. The k_{trans} values were 3.56 x 10^3, 4.0 x $10^{3,}$ and 8.73 x 10^3 s^{-1} for Device N, P, and N+P, respectively. The k_{rec} values were 180, 195, and 144 s^{-1} for Device N, P, and N+P, respectively. From both analyses, it is clear that Device N+P supports efficient charge transport to a great extent and suppresses charge recombination with the help of the generated internal dipole.

2.10 Bi-based PSC: Alternative to Pb-based PSC

Chen et al. used $CsSnI_3$ as a potential candidate for perovskite active layers. However, a very low PCE of 0.9% was obtained [30]. Noel et al. [31] further developed Sn-based PSCs and changed them to CH_3NH_3 to get a PCE of 6%. $CH_3NH_3Pb(I_{1-x}Cl_x)_3$ also is a recently developed material with a similar bandgap to $CH_3NH_3PbI_3$ but with a higher PCE because of the better charge diffusion properties. Similar material was used, $CH_3NH_3PbBr_3$. The resulting device had improved V_{oc} but with a wider bandgap, leading to lower absorption in the visible region. Hybrids, including $CH_3NH_3Pb(I_{1-x}Br_x)_3$, resulted in a device with a PCE of 17.9%. Bi-based PSCs are currently being actively studied and researched due to the toxic-free nature that can be harnessed to replace Pb-PSCs [32, 33]. Its unique properties, high carrier lifetime, and improved stability against air and extrinsic factors make this material a favorable candidate for Pb-based PSCs. Moreover, the ability of Bi-PSCs to absorb radiations in infrared and visible regions of light gives it an added advantage and is eco-friendly. The issue with Bi-perovskites is the indirect bandgap which calls for thicker layers of the film, thus, reducing the mobilities of charge carriers [34]. Ismail Benabdallah and co-workers analyzed the properties (photovoltaic and non-photovoltaic) of $CH_3NH_3BiX_3$ where X = I_2Te, I_2S, and I_2Se [35]. Table 3 elucidates the tolerance and octahedra factors of different perovskite molecules.

The geometry of $CH_3NH_3BiX_3$ materials was analyzed to $CH_3NH_3PbI_3$, hoping that the obtained data will have a more stable structure than the latter. The tolerance and octahedra factors were calculated. The octahedra factor is calculated using the following formula:

$\mu = R_B/R_x$, where $\mu > 0.41$ is considered a stable structure.

Table 3. Tolerance and Octahedra Factor for various Perovskite structures

	$CH_3NH_3PbI_3$	$CH_3NH_3BiI_2Te$	$CH_3NH_3BiI_2Se$	$CH_3NH_3BiI_2S$
Tolerance Factor	0.95	0.99	1	1.01
Octahedra Factor	0.54	0.46	0.51	0.50

The tolerance factor was found to be 0.95, 0.99, 1 and 1.01 for $CH_3NH_3PbI_3$, $CH_3NH_3BiI_2Te$, $CH_3NH_3BiI_2Se$ and $CH_3NH_3BiI_2S$, respectively. The octahedra factor was found to be 0.54, 0.46, 0.51 and 0.50 for $CH_3NH_3PbI_3$, $CH_3NH_3BiI_2Te$, $CH_3NH_3BiI_2Se$ and $CH_3NH_3BiI_2S$, respectively. Hence the values validate that all the analyzed materials are perovskite types. The variation of A cation (CH_3NH_3) and its distribution do not impact the bond lengths and angles except for a slight molecular arrangement. This distortion can be attributed to the loose interactions between the organic-inorganic hybrid. Moreover, the lattice constants in all the materials are nearly constant when compared to $CH_3NH_3PbI_3$ due to the similar size parameter (ionic radii) of Pb and Bi. The VBM of $CH_3NH_3PbI_3$ has strong Pb-s and I-p antibonding characteristics. The CBM has strong Pb-p characteristics, thus, showing the dual nature (ionic and covalent) of halide perovskites. A similar observation can be seen for $CH_3NH_3BiI_2Te$. The bandgap obtained from analysis for $CH_3NH_3BiI_2Te$ is found to be 0.84 eV. However, it is essential to note that this material has an indirect bandgap which can be related to the presence of T_e.

Similarly, $CH_3NH_3BiI_2Se$ has a slightly better bandgap of 1.15 eV but with an indirect bandgap. The only material that made a clear exception was $CH_3NH_3BiI_2S$ is 1.30 eV which is direct bandgap material with a value relatively closer to $CH_3NH_3PbI_3$ of 1.50 eV. For Bi-based perovskites, the band structure depicts that the VBM is dispersive but less than $CH_3NH_3PbI_3$. The VBM looks a little flatter. This can be related to the T_{e-p} orbitals on top of the valence band, which shows that the hole's mass is greater than the electron's mass. There is an antibonding s-p coupling taking place along with this that allows enhanced diffusion lengths for charge carriers. A similar phenomenon can be related to $CH_3NH_3BiI_2Se$ and $CH_3NH_3BiI_2S$. On conducting an optical analysis, it was observed that Bi absorption characteristics include visible and IR regions due to I-5p valence and Bi-6p absorption states. The optical transition of Bi-6s states near Bi-6p conduction states is also responsible for this property. On studying the charge density for all the compounds, the octahedra distortion and ionic bonding in $CH_3NH_3PbI_3$ are weaker when compared to Bi-based perovskites. Higher interaction was observed for Bi-S than Bi-I, responsible for better stabilization characteristics. This again can be related to Bi-Te and Bi-Se thus, as stated before, Bi can be considered mainly for replacing the toxicity problem of Pb and having improved absorption properties.

2.11 Air Stable Organic-Inorganic Bi-PSCs

MA3Bi2I9 (MBI) perovskite layers have high porosity and low substrate wetting capacity [36]. Singh et al. [37] showed that perovskite films could possess a unique needle-like structure. This proved that film morphologies and homogeneity played an essential role in determining the PCE of the device up to 0.2%. In this work, we will be looking into the activities of S. Sanders and co-workers where the concentration of the MBI precursor solution was varied, and its impact on photovoltaic parameters and device lifetime was evaluated. The device's architecture used is FTO (F-doped SnO_2)/c-TiO_2/m-TiO_2/MBI/Spiro-OMeTAD/Au. The device had an active surface area of 0.25cm^2 [38].

In this work, the concentration of the perovskite precursor solution is varied from 0.15 to 0.30 M in intervals of 0.5 M. The dependence of the perovskite concentration solution is studied to understand the impact on crystal growth size and rate. From the SEM analysis, the layer thickness of the MBI film varied from 180 to 300 nm as the precursor solution concentration increased from 0.15 to 0.30 M, respectively. Nine devices of the above architecture were produced to test the reproducibility and performance characteristics. Before studying the PV and IV characteristics of the produced devices, they were exposed to the ambient atmosphere for two days, thus, yielding maximum PCE, J_{sc}, and V_{oc} values. Figure 9 shows the device architecture and constituents of the fabricated device using Bismuth.

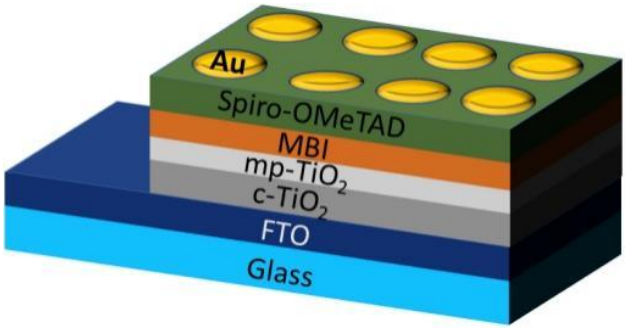

Figure 9. PSC Device architecture using Bi-based Perovskite

The concentration of the initial precursor solution has a considerable effect on the crystalline size, the number of nucleation sites, and the growth rate. Maximum crystal size of 1 µm was obtained for 0.20 M perovskite concentration. As the concentration increases to 0.25 and 0.30 M, the nucleation rate increases, restricting lateral crystal growth. Hence, in both extremes of the perovskite concentration, the crystal size is lesser than the median concentration of 0.20 M. Small crystal size (300 nm) for 0.15 M perovskite precursor concentration is a lower concentration does not provide a reasonable growth rate. The obtained V_{oc} values were around the value of 0.72 and 0.73 V, except 0.15 M. It is important to note that these obtained V_{oc} values are the highest obtained for this type of device. The low value for 0.15 M can be attributed to the reduced perovskite coverage these films offer, thus, creating more paths for shunting. As a result, parasitic recombination of charge carriers and the presence of dark current can potentially reduce the device's performance, which eventually minimizes the V_{oc} value. The rising concentration of perovskite precursor increases the

film thickness significantly. The increase in film thickness increases the film's series resistance and the device as a whole. This, in turn, reduces the FF value of the device, which can be seen in the table above. The dependency of J_{sc} can be attributed to the crystal size of the film. The larger the crystal size, the greater the J_{sc} value obtained. This is because of the reduced charge trapping at grain boundaries. On comparing the various perovskite precursor concentrations, the device with 0.20 M has the highest average J_{sc} value of 0.61 mA/cm^2 and an average PCE value of 0.169%. Table 4 shows the variation of photovoltaic performance as a function of precursor solution concentration.

Table 4. Photovoltaic performance of varying precursor concentration

Concentration (M)	J_{sc} (mA/cm^2)	V_{oc} (V)	FF (%)	PCE (%)
0.15	0.48	0.633	39.15	0.119
0.20	0.61	0.719	38.47	0.169
0.25	0.52	0.749	36.07	0.140
0.30	0.39	0.717	33.12	0.094

The stability measurements are analyzed along with performance characteristics. Three samples of optimized 0.20 M precursor solution were taken. Sample A (reference sample) was stored in purified N_2 and a mixture of H_2O and O_2 at less than ten ppm. Sample B was stored in the air. For sample C, the perovskite layer on TiO_2 was initially exposed to air for 48 hours before fabricating the device with Spiro-OMeTAD and Au. Sample C was stored in ambient air. The stability measurements of all the samples were taken in an N_2 atmosphere under unencapsulated conditions. A standard measurement seen for all the samples was the low PCE values, lesser than 0.03%. Only sample A showed a visible increase in performance after 11 days due to an increase in V_{oc} value. This can be related to the doping of Spiro-OMeTAD film with residual O_2 molecules in the atmosphere of N_2. A similar principle can even be noticed where Spiro-OMeTAD gets influenced by Li-TFSI and O_2 to reach a p-type doping level with a PCE of 10% with improved conductivity. This same phenomenon can be observed in sample B. The highest obtained PCE after 48 hours of storage was 0.16% which dropped to 0.09% after 13 days. This can be attributed to the J_{sc} and V_{oc} reduction values due to atmospheric degradation in the presence of moisture. A low PCE is observed immediately after a modified fabrication process for sample C. The initial performance of the device was not improved; thus, one can conclude that Spiro-OMeTAD-based doping of O_2 can improve the PCE. After 48 hours, the PCE was found to be 0.11%, which was lower than a device without the modified-fabrication process. From the above results, it is more than evident that MBI-based perovskites have broad prospects in the future and can prove to be a fruitful alternative to inexpensive solar cells.

2.12 Bi-based Perovskite using Solvent Engineering

The need for eco-friendly alternatives for PSCs fabricated using non-toxic solvents is the need of the hour for producing PSCs on a commercial scale [39]. Wang et al. [40] previously showed that different solvent compositions of DMSO/1-pentanol (1-P)/2-dimethylaminoethanol (2-MP) could impact the perovskite film quality and crystal arrangement and orientation. An efficient device was produced when reducing the high boiling point substance of DMSO. Thus, this strategy showed that DMSO/1-P/2-MP solvents could produce high-efficiency PSCs. Ramadan et al. showed that using a solvent system of methylamine (MA)/acetonitrile (ACN)/dimethylformamide (DMF) produces a $MAPbI_3$ film rapidly under room-temperature conditions [41]. However, DMF solvent has severe problems. One of the significant issues is the toxic and volatile nature that hinders it from mass commercialization. $MABi_2I_9$ is a unique perovskite material that is heavily researched due to its moderate bandgap of 1.9 eV, high electron and hole mobility values, significant absorption coefficient, lower surface recombination, and long electron and hole diffusion lengths. The solvent used for fabricating the perovskite film influences the film formation and quality of the film for further processing. Some commonly used solvents are DMSO, DMF, and Gamma-butyrolactone (GBL) [42]. Solvents can be either polar or nonpolar. Further, polar solvents can be classified into protic and aprotic solvents. Protic solvents can form hydrogen bonds due to the availability of at least one hydrogen. Some examples include water, ethanol, methanol, etc. Aprotic solvents do not contain free hydrogen that can form hydrogen bonds. These include molecules like DMSO, DMF, CAN, GBL, etc. In this section, we will be looking into the works of Muhd Sahrul Nizam Sahul Hameed and his co-workers. They aim to improve the film quality of Bi-perovskites using non-toxic solvent engineering procedures [43]. The optimum volume ratio used to prepare the precursor solution of various solvents is shown in Table 5.

Table 5. Volume % of solvent required for precursor solution

Solvent	Volume (%)
DMSO	100
DMSO/ACN	70/30
DMSO/MA	70/30
DMSO/ACN/MA	50/20/30

When preparing perovskite films through a one-step solution processing method, the perovskite precursor solution is mixed with appropriate solvents before spin-coating it on the substrate. Once this mixture is deposited, the substrate undergoes thermal annealing. After surpassing the transition point, the solvent evaporation rate suppressed the film thinning process. This evaporation rate is governed by the solvent's vapor pressure and boiling point. Table 6 elaborates on the physical properties (Vapor Pressure and Boiling Point) of each of the solvents used.

On analyzing all the samples after thermal annealing, it can be concluded that all films had a yellowish-orange color pre-annealing. Post-annealing, all films possessed a similar color with a dark brownish shade. It was found that DMSO yielded poor perovskite films with low surface wettability and coverage. This is because of DMSO's high boiling point and low vapor pressure, which increases the drying time with a

reduced evaporation rate during the fabrication process. MA yielded a high-quality perovskite film with a comparatively better surface morphology and homogeneity. This can be related to MA's low boiling point and high vapor pressure, accelerating the evaporation rate. Similarly, ACN produced a comparatively better quality of perovskite film due to its lower boiling point when compared to DMSO.

Table 6. Physical properties of each solvent type

Solvent	Vapor Pressure (T = 25°C, kPa)	Boiling Point (°C)
DMSO	0.08	189
MA	28.8	56.9
ACN	9.9	82

It is evident that when using a film of DMSO/ACN/MA, the film obtained will have the best quality with improved surface coverage and wettability. This is because the obtained film has the intermediate properties of all the solvents. It is important to note that the one-step solution processing method has a few inherent drawbacks, such as the difficulty in regulating the thickness of the film, control of film morphology, rate of film formation, etc. Since the method's drawbacks cannot be changed, the materials used in fabrication can be modified. Various solvents can improve wettability and modify surface deposition rate, crystal growth kinetics, and perovskite coverage. These minute parameters can eventually scale to impact the device's stability and overall performance to a great extent. The UV-Vis absorption spectra were studied, and the results were analyzed. It can be seen that there is a broad absorption region ranging from the infrared region (NIR) to the visible region, thus, indicating the presence of Bi in the perovskite film. The maximum absorption wavelength is approximately 490 nm for all the samples. It was observed that a maximum absorption characteristic could be observed for DMSO/ACN/MA film due to its better surface coverage, improved film morphology, and enhanced film quality and homogeneity. The optical bandgap for the perovskite material using DMSO/ACN/MA was approximately equal to 1.9 eV, which was determined using Tauc's plot. The high absorption coefficients of the materials confirmed the direct bandgap property of these materials. The following direct transition state was evaluated to be at approximately 2.35 eV. A solid and broad excitonic absorption peak at 500 nm is observed for the DMSO film. Further analyzing the DMSO film, we observe that the absorbance range of this film is comparatively lower because of its low surface coverage and nucleation rate. The PL measurements were taken, and it was evident that PL intensity for DMSO film was higher when compared to DMSO/ACN/MA film and had a better quenching effect. These results clearly show that modified and regulated solvent engineering can reduce the non-radiative recombination of the perovskite film. This lower non-radiative recombination can subsequently lead to higher charge transfer rates which further improves the device's performance. Thus, from solvent engineering, we can effectively conclude that using solvents at optimum concentrations can produce highly efficient films for photovoltaic applications. Furthermore, using non-toxic solvents, which can be additional modified using solvent engineering, can improve the performance of a PSC device and be the next step for the commercialization of photovoltaic technologies.

2.13 Silver Bismuth Iodide for High-efficiency

As discussed previously, the replacement of Pb with transition metals such as Sn^{2+} or Ge^{2+} can minimize the toxicity level. However, it has been studied that PSCs manufactured from these materials are often very unstable [44]. Using the 2D/3D strategy in perovskites, the highest performing Sn-based PSC retained only 50% of its initial PCE after three days under 20% RH [45]. One strategy that can be used is the usage of trivalent cations like Bi and Sb is a possible alternative because of their low toxicity and high atmospheric stability [46]. Using cations like MA or Cs with Bi has given promising results, high absorption coefficients, and solution processing ability. However, the usage of such materials results in poor electrical dimensionality and high optical bandgap [47]. In order to improve the dimensionality of the perovskite material, one such strategy can be the alteration of the A-site cation by varying it with cations like Ag or Cu. Using either Ag or Cu can reduce the optical bandgap and give a rigid 3-dimensional octahedral network. Iodobismuthates are materials that have shown superior electrical conductivity and optoelectronic properties. The first application of these compounds was shown by Sargent and co-workers with $AgBi_2I_7$ perovskite active layer to get a PCE of 1.22% [48]. Zhu et al. [49] later optimized this, where Ag_2BiI_5 was used as the active layer to get a PCE of 2.1% in a mesoscopic solar cell architecture prepared under an inert atmosphere. In this section, Ghosh and co-workers used a dynamic hot casting (DHC) method to fabricate Bi-based PSCs using $AgBiI_4$ and Ag_2BiI_5 in a mesoscopic device architecture [50]. Unlike other fabrication methods, the devices, in this case, were fabricated under ambient conditions using a single-step spin coating mechanism without any antisolvent treatment. DHC is when a hot precursor solution is dropped onto a preheated substrate surface during the spin coating stage. Such a method could produce pinhole-free and uniform morphology perovskite films with sufficiently large crystalline grains. DHC also enabled a better regulation over stoichiometry as AgI has poor solubility in solvents like DMSO and DMF at room temperature.

As per reports, there are four ternary states of Ag-Bi-I systems, namely, $AgBiI_4$, Ag_3BiI_5, Ag_3BiI_6 and $AgBi_2I_7$. Out of the four states, $AgBi_2I_7$ was energetically unfavorable. Ag_3BiI_5 and Ag_3BiI_6 have similar geometry (trigonal structure) and similar lattice constants. Ag_2BiI_5 state was only capable of producing thin films despite the variation in precursor concentration. The results from Jung et al. validated this finding. On increasing the Ag:Bi molar ratio, the XRD patterns showed increased diffraction patterns for the unreacted AgI present. However, increasing the precursor concentration in a non-stoichiometric manner resulted in the recrystallization of $AgBiI_4$. There were trace impurities present, which can be attributed to BiI_3 or Ag_2BiI_5. The SEM analysis was conducted, and the results were compared to films fabricated by the

Normal Spin Coating (NSC) method. The results showed that the thin films obtained by the DHC method had better morphology and large crystal size when compared to NSC. This can be due to the better control that the DHC method provides over the local supersaturation of the precursor solution. For Pb-halide perovskites, the level of local supersaturation was determined by antisolvent treatment. In conventional antisolvent treatment, the solubility of the precursor is high at the beginning. When depositing the solution on the substrate, the antisolvent is suddenly deposited at the beginning. This results in reduced solubility of the precursor solution. Consequently, more excellent nucleation, uniform morphology, and compact films are produced, giving a higher performance for Pb-based perovskite films. However, when this similar process was replicated for Bi-halide perovskites, the formation of pinholes and voids was very prominent. The possible explanation for this can be due to the rapid crystallization rate of Bi-perovskites. The DMSO solvent could have been entrapped in the film. Thus, while pursuing this sort of treatment, the film produced had poor morphology. This phenomenon was observed for both DHC and NSC methods. For the DHC method, the nucleation does not begin when the solution is hot at high temperatures. Before depositing the precursor solution, the centrifugal force of the spinning method removed the solvent, resulting in a supersaturated solution above the TiO_2 surface. As this continued, one could notice the layer-like formation between the different layers present in the device. Grain growth and nucleation began immediately after the annealing process. Hence, from this finding, we can conclude that TiO_2 behaves as a nucleation site for the DHC method, resulting in uniform and compact films. The absorption spectra of $AgBiI_4$ and Ag_2BiI_5 films by NSC and DHC methods were studied. The absorption characteristics of both films were similar. However, films produced through the DHC method showed higher absorption capabilities in the reduced number of pinholes and voids than the NSC method. T bandgap was approximately 1.66 and 1.7 eV for $AgBiI_4$ and Ag_2BiI_5, respectively, through an indirect bandgap relation. The absorption spectra for Ag_4BiI_7 showed a peak at 3 eV. This abnormal behavior can be related to the presence of AgI, as shown in the XRD analysis. None of the films impacted conducting the photoluminescence measurements, thus confirming the indirect bandgap nature. The charge transfer kinetics were observed using Transient Absorption Spectroscopy (TA). This analysis showed that films produced by NSC and DHC have similar charge transfer dynamics. The TA spectra showed a strong photobleaching effect around 2.1 eV and 2.05 eV for $AgBiI_4$ and Ag_2BiI_5 films, respectively, along with a photo-induced absorption peak at higher wavelengths. The PB behavior is related to the indirect bandgap nature of these materials where the change of state of charge carriers from a relaxed state to the indirect bandgap edge. The direct bandgap for these materials was found using Elliot's equation. Figure 10 gives a clear representation of how a device is fabricated using the DHC method. The approximate direct bandgap was 2.37 and 2.2 eV for $AgBiI_4$ and Ag_2BiI_5. The exciton binding energies corresponding to the direct property were 260 and 150 meV for $AgBiI_4$ and Ag_2BiI_5, respectively. The decay dynamics were analyzed and fitted with a bi-exponential decay formula. The parameters are summarized as follows: for NSC films, the T_1 values were approximately equal to 7 and 12 ns, and T_2 values were approximately equal to 23 and 83 ns for $AgBiI_4$ and Ag_2BiI_5 films, respectively. For DHC films, the T_2 values were approximately equal to 75 and 133 ns for AgBiI4 and Ag_2BiI_5, respectively. When comparing the absorption edge of the films, DHC-fabricated films have a steeper slope than NSC. The reason for this is the reduced structural disorder. DHC-fabricated films possess a greater carrier lifetime and absorption because of their reduced trap density and larger grain size, related to the film's passivation effect and smooth morphology. The carrier density was 4.21 x 10^{14} and 3.91 x 10^{14} cm^{-3}. The carrier mobility was 1.74 and 2.26 $cm^2V^{-1}s^{-1}$ for $AgBiI_4$ and Ag_2BiI_5 films. To quantify the photovoltaic performance of these films, a device with the following architecture, FTO/c-TiO_2/m-TiO_2/Active Layer/PTAA/Au, was fabricated. Using UPS measurements, the VBM was determined to be -5.5 and -5.7 eV for $AgBiI_4$ and Ag_2BiI_5 films, respectively. Similarly, the CBM was determined to be -4.0 and -3.8 eV for $AgBiI_4$ and Ag_2BiI_5 films, respectively, using optical bandgap values. The photovoltaic parameters of NSC and DHC devices are recorded in the table below. It is important to note that the devices were fabricated under 65% RH ambient conditions. In contrast, other studies used devices fabricated and stored under expensive glove boxes filled with inert gas. The solar cells fabricated through DHC had higher V_{oc}, J_{sc}, and FF values.

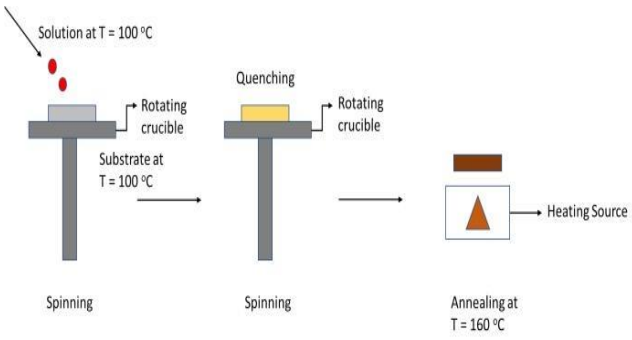

Figure 10. Pictorial Representation of Dynamic Hot Casting Method

The highest obtained PCE from $AgBiI_4$ and Ag_2BiI_5 solar cells using the DHC technique are 2.18% and 2.62%, which is the highest recorded efficiency for an Ag-Bi-PSC solution-processed. Moreover, along with producing promising efficiencies, the devices had a high reproducibility and negligible hysteresis. The IPCE (Incident Photo to Current Conversion Efficiency) measurements were recorded at 300 to 750 nm for $AgBiI_4$ and Ag_2BiI_5. The integrated current densities were 6.6 and 7.9 mA/cm^2 for $AgBiI_4$ and Ag_2BiI_5 films. These results show that the films perform better under low-intensity radiation. The variation with J_{sc} and V_{oc} was taken with light intensity to understand the device's performance concerning light further. The current and intensity relationship showed a sublinear pattern with saturation at higher intensities. This indicates that charge collection efficiency significantly decreases at higher light intensity. This could be the inadequate charge collection ability due to the device's non-optimal thickness and carrier mobility of HTM and ETM. A semi-log plot between V_{oc} and

light intensity was plotted with a slop of 1.5kT/q. This result shows that, near V_{oc} value, heavy recombination is observed due to traps. As a result, a variation of FF with light intensity was studied, and a maximum FF of 68.6% at 31.6 mW/cm^2 intensity was obtained. This predominantly indicates that at lower intensity radiation, the recombination is reduced, and charge collection efficiency is enhanced. The devices were stored in an ambient atmosphere at 20^{o}C with an RH of 60-75% to account for the stability characteristics. This device remained stable for over a month, with the V_{oc} showing little to no variation. However, there was a notable drop in J_{sc} and PCE values due to the rapid degradation of the HTM. From the results listed in Table 4, we can confirm that the DHC technique enables a faster crystallization rate, large crystal size (microns), and rapid removal of precursor solution, which provides improved photovoltaic performance than conventional methods for Bi-based PSCs. These devices performed exceptionally well under low-intensity light conditions, showing the usage of indoor applications. Possible research and modifications can improve the PCE of these devices to even greater extents.

2.14 Cu(II) Phthalocyanines as an HTM

High-performance PSCs use HTMs that efficiently transport holes and block electrons to reduce recombination to get higher PCE. It is also necessary that when the HTM is in a p-i-n configuration, the material should have strong stability characteristics with hydrophobic properties. However, using conventional HTMs, the stability and preparation methods are pretty tricky. Metal phthalocyanines have been regarded to possess suitable hole-transporting properties and highly stable, low-cost, and easy preparation methods. Previous studies have been done on these materials to get PSCs of PCEs up to 16% [51-54]. In this section, Yulong Wang and co-workers have fabricated a Copper (II) Phthalocyanine (CuPc), tetra-methyl Copper (II) Phthalocyanine (CuMePc), and tetra-ethyl Copper (II) Phthalocyanine (CuEtPc) by vacuum deposition [55]. It has been studied that the usage of tetra-alkyl groups as an HTM is favorable for appropriate hole transport properties, hydrophobic properties, and improved performance. The device's architecture used in this section is FTO/SnO_2/$MAPbI_3$/HTM/Au, with an active area of 0.11 cm^2. SnO_2 is because of the lower processing temperatures (<180 ^{o}C) than TiO_2.

Table 7. Device performance varying with fabrication method and perovskite material

Technique	Material	J_{sc} (mA/cm^2)	V_{oc} (V)	FF (%)	PCE (%)
NSC	$AgBiI_4$	3.70	0.63	51.40	1.2
NSC	Ag_2BiI_5	4.42	0.63	57.60	1.6
DHC	$AgBiI_4$	5.24	0.67	62.09	2.2
DHC	Ag_2BiI_5	6.04	0.69	62.40	2.6

Table 7 shows the variation of photovoltaic output parameters with device fabrication techniques. To test the thermal stability of CuMePc and CuEtPc, TGA was conducted. The weight loss of the material films was studied with rising temperatures. It was found that there was a significant change in mass for temperatures greater than 500^{o}C. The Td temperature was 550 ^{o}C, 525 ^{o}C and 510 ^{o}C for CuPc, CuMePc and CuEtPc, respectively. These results show that Pc-based films have high thermal stability when fabricated from thermal vacuum deposition. The presence of alkyl chains influenced the absorption spectra significantly. The CuPc film has a double absorption peak observed at 624 nm and 695 nm in the visible region, showing the π-π* transition. When heating the CuPc film, the peaks observed in higher intensity are more miniature, indicating the transition of CuPc from α to β phase, thus facilitating hole transportation.

Similarly, for CuMePc and CuEtPc films, the heating treatment reduced the intensity of peaks at 692 and 690 nm. The molecular packing of the films was analyzed using Grazing Incidence X-Ray Diffraction (GIXRD). The HTMs were deposited on a SiO_2/Si substrate showing signals at 2θ values of 6.86^o, 6.05^o, and 5.78^o for interplanar distances of 12.85 A^o, 14.61 A^o, 15.09 A^o for CuPc, CuMePc and CuEtPc films respectively. The results also indicated that CuPc films consisted of a molecular arrangement with an 83.2^o tilt angle. Their molecules aligned nearly perpendicular to the substrate. Similarly, for CuMePc and CuEtPc, the molecular lengths were 16.1 A^o and 18.4 A^o with an intense π-molecular stacking and a tilt angle of 77.7^o 73^o, respectively. On conducting an Organic Field-Effect Transistor analysis, the mobility values varied greatly. The hole mobility of CuPc was 1.8 x 10^{-4} cm^2/V and a threshold voltage of -4.4 V. The charge mobility of CuMePc was found to be 6.1 x 10^{-4} cm^2/V, and a further increase in alkyl chains reduced the hole mobility, where CuEtPc had hole mobility of 3.8 x 10^{-4} cm^2/V. The Space-Charge Limited Current (SCLC) mobility measurements determined all the films' charge transport dynamics. The CuMePc film showed the highest SCLC mobility of 1.95 x 10^{-3} cm^2/V, and an increase in alkyl chains reduced the SCLC mobility (CuEtPc = 3.75 x 10^{-4} cm^2/V), which can be validated using the OFET analysis and lastly, the SCLC mobility of CuPc was 7.45 x 10^{-4} cm^2/V. As per the Selected Area Electron Diffraction (SAED), the improved transistor mobility can be attributed to intermolecular solid π-π interactions present in the sample. Alkyl sidechains contribute significantly to charge transport and tune the molecular interactions, consequently modulating the film morphology. Even subtle variations like sidechain engineering, backbone engineering, chain length variation, etc., can impact the charge mobility. However, on increasing the number of alkyl sidechains, two notable phenomena occur intermolecular dispersive attraction and steric hindrance. On attaching alkyl sidechains to the backbone, the number π-π stacking distance decreases, and the π-π molecular interaction increases, which improves charge mobility. However, with an increase in alkyl chains, the bulky nature of these molecules reduces the charge transport. The increase in alkyl chains also increases the vibrations within the molecule, which further disturbs the molecular arrangement of the film. These theoretical concepts completely agree with hole mobilities obtained when transitioning from CuMePc to

CuEtPc. Figure 11 is the depiction of the device architecture and energy band alignment of all the materials used in the PSC.

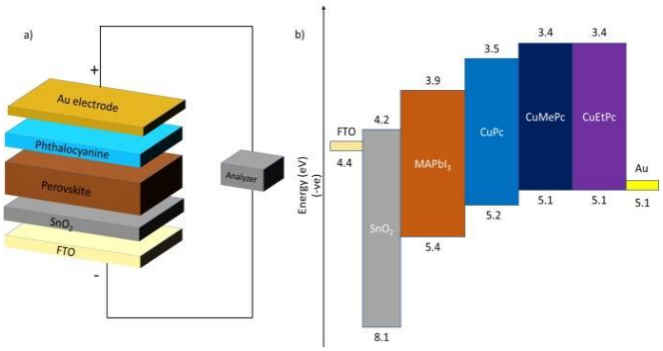

Figure 11. PSC Device structure with Phthalocyanine as HTM, b) Energy Band alignment of all materials used in PSC

On analyzing the energy band levels, the HOMO levels of the HTM were well-matched with the perovskite and Au energy level. Even the LUMO levels of the HTM were suitable for perovskite and FTO energy bands. These results show that there can be efficient hole extraction from perovskite to the HTM and hole injection from HTM to the Au. Similarly, the electron transfer can be blocked at the interface and thus reducing charge recombination to a large extent. The PL spectra of the perovskite films coupled with the HTM are conducted. The quenching effect is observed to be 92.6%, 97.7%, 98.7% and 98.1% for reference Spiro-OMeTAD, CuPc, CuMePc and CuEtPc, respectively. These results show that Pc-based films are more favorable HTMs due to their efficient charge transporting properties, attributed to the alkyl substitution on Pc.

The photovoltaic performance of the device is recorded under AM 1.5, 100 W/m^2 artificial light simulation. Moreover, ten devices of each HTM type were fabricated to record the average and highest PCE. The CuMePc showed the highest values of J_{sc} with an average photovoltaic performance of, Jsc = 23.11 mA/cm^2, V_{oc} = 0.968 V and PCE = 11.7%. CuPc showed an average performance of J_{sc} = 23.08 mA/cm^2 and FF = 43.5%. Lastly, CuEtPc shows the least performance with J_{sc} = 22.81 mA/cm^2 and FF = 49.9%. These performance values are in complete agreement with the obtained SCLC values. The V_{oc} values of CuMePc and CuEtPc were also comparatively higher when compared to CuPc. This can be related to the spacer effect of the alkyl substitution. The IPCE analysis was also done to analyze the performance of the device. The results obtained from IPCE measurements completely agree with the previously conducted tests. An enhanced IPCE value was observed in the visible region (300-800 nm). The CuMePc device had higher values of IPCE when compared to CuEtPc and CuPc-based devices.

Metal phthalocyanines have been regarded for their excellent stability characteristics. In some cases, they have been found ideal as an encapsulant. The air stability of the devices was tested under ambient conditions at 25 ^oC and 70% RH, with a continuous evaluation every 24 hours. After ten days, the CuPc-based device could only retain 16.6% of its initial PCE. The CuMePc device could retain 33.6% of its initial PCE, whereas the CuEtPc device retained 88%. It is important to note that the PCE, V_{oc}, $J_{sc,}$ and FF values in the CuEtPc-based device showed the highest stability with little fluctuation over time. For CuMePc and CuPc devices, the V_{oc} and J_{sc} values decreased as time proceeded. It was necessary to study it concerning a Spiro-OMeTAD-based device to predict the optimum device performance. The device's architecture used in this case was FTO/SnO_2/Perovskite/Spiro-OMeTAD (Li-TFSI doped)/Au. This device showed an average PCE of 12.83%. On conducting the stability test for such a device, the V_{oc}, J_{sc}, FF, and PCE values dropped extremely fast after five days of storage which showed the better stability properties of Pc-based devices. This poor stability of the spiro-OMeTAD-based device is because of the moisture infestation into the device. The degradation measurements of all devices were recorded with and without HTMs every 48 hours using UV-Vis absorption and XRD analysis. Before exposure to the moisture, all the samples showed a glossy brown color. PSCs without the Pc-HTM experienced moisture degradation after two days of exposure. The film turned to brown color after ten days of exposure. Whereas, for devices with CuPc, CuMePc, and spiro-OMeTAD, significant degradation began only after six days, and in the case of CuEtPc, very few degradation effects were seen after ten days of exposure. The XRD results analysis confirms these findings where PbI_2 is formed as an impurity under exposure to moisture. It is evident that, long-term operational stability will follow the order: CuEtPc > CuMePc > CuPc > spiro-OMeTAD. The grain sizes of these films showed a dense and compact film packing with smooth morphology and large grain boundaries. The average and RMS grain size was nearly 200 and 5.45 nm, respectively. It was determined that there is a dependence of alkyl chains on grain sizes. CuPc film showed loosely packed grains with an average size of 150 nm. CuMePc had a tighter arrangement and condensed film structure with an average grain size of 150 nm. CuEtPc film did not have grains, but plate-like structures of ~500 nm were observed, which provided the device with better film coverage. Moreover, the moisture stability and the carbon atoms' dependency can be studied. As the number of carbon chains/atoms increases, the hydrophobicity increases, providing CuEtPc with its highly stable nature. The contact angle of water was 80.5^o, 92.3^o, 105.6^o, and 65.5^o for CuPc, CuMePc, CuEtPc, and spiro-OMeTAD, respectively. The larger the water contact angle, the higher the hydrophobicity and more excellent stability against moisture and humidity. This study shows that the Cu (II) phthalocyanine with side-alkyl chains can be the next innovation for dopant-free HTMs. The addition of alkyl chains significantly improved the carrier properties, hydrophobicity, and long-term stability of the device. Since FF values of these devices are low, further research needs to be conducted on how one can optimize these values to a greater extent using suitable engineering techniques.

2.15 Copper (I/II) Porphyrin HTM

Spiro-OMETAD has been one of the most used HTMs for PSCs. However, the low hole mobility and electrical conductivity restrict all devices' mass implementation. Using dopants such as 4-tert-butylpyridine (TBP) and bis(trifluoromethane) sulfon-imide lithium salt (Li-TFSI) can tune the properties of spiro-OMeTAD. Li-TFSI is, unfortunately, hydrophilic. Thus, it tends to absorb moisture

from the atmosphere to impact the device's performance in a negative manner [56]. Additionally, the cost of spiro-OMeTAD is higher than that of gold and platinum. Thus, using additional dopants will increase the cost of fabrication, which is illogical. The next step is to discover alternate HTMs that can be comparable to the performance of spiro-OMeTAD or even better. Researchers have designed various organic, inorganic, conjugated polymers and coordination compounds. Copper complexes of bis (2,9-dimethyl-1,10-phenanthroline) and copper(I/II) [CuI/II(dmp)$_2$] have been used as a redox electrolyte in DSSCs previously. These copper complexes have a high self-exchange rate between Cu(I) and Cu(II) oxidation states for electron transfer. Porphyrin and its derivatives are electron-rich and have strong π-π molecular stacking properties and varied photophysical and electrochemical properties. The efficient charge extraction and conversion giving rise to high PCEs that porphyrins have shown with DSSCs make it ideal for HTMs in PSCs [57, 58]. Zhu's group showed that using Copper porphyrin, which is dopant-free, produced devices over 17% PCE [59]. The slightly lower performance is due to lower solubility levels in chlorobenzene, which can be altered by molecular construction. The Cu center and the high self-exchange rate between Cu(I) and Cu(II) complex can have high charge transfer rates. Along with the acylhydrazone group and Cu center, the interfacial recombination can be significantly reduced and consequently improve cell performance. In the following section, chang-Dai Si and coworkers developed a facile synthetic method to make an acylhydrazone group substituted with Cu porphyrin, termed CuP [60].

The device architecture used by Chang-Dai Si and coworkers is a mesoporous form of FTO/TiO_2/$MAPbI_3$/HTM/Au. Both spiro-OMeTAD and CuP HTMs are used to do a comparative study. UV-Vis absorption spectra showed two notable absorption bands at 420 nm and 544, 586 nm. These results show that CuP has little to no competitive absorption with the perovskite active layer. Further, the UV-Vis absorption spectroscopy study was conducted for the perovskite/HTM arrangement. A higher intensity was observed for the perovskite/CuP arrangement before 485 nm, which gradually decreased until 800 nm. Cyclic voltammetry measurements are done in DMF solution with 0.1 mM TABF6 as an electrolyte in a 3-electrode system to test the redox energies of the HTMs. The HOMO energy level of CuP is above the perovskite layer (-5.43 eV), which can create sufficient driving force for efficient hole injection into the electrodes. The photovoltaic performances of the devices were measured under AM 1.5, 100 mW/cm^2. The CuP device had a PCE = 18.21%, J_{sc} = 22.57 mA/cm^2, V_{oc} = 1.10 V and a FF = 73.34%. The porphyrin maintained a similar structure, but Zn replaced the metal center to give ZnPy-based PSCs. The output obtained from this device is PCE = 17.82%, J_{sc} = 22.29 mA/cm^2, V_{oc} = 1.09 V and FF = 73.12%. The high self-exchange rate between Cu(I) and Cu(II) makes CuP an ideal HTM over ZnPy and, hence, higher performance. The charge transfer and mobility characteristics can be measured through the EIS measurements. The higher R_{rec} and R_{tr} values for CuP-based PSCs than spiro-OMeTAD-PSCs indicate the efficient hole extraction and transfer along with reduced charge recombination probability. The PL measurements were taken to study the charge transfer dynamics using the HTM/perovskite/glass architecture. The reduced PL intensity for CuP-PSCs shows the improved hole extraction and transfer from the perovskite layer to the HTM layer. The quenching effect of CuP is similar to spiro-OMeTAD, which shows a similar charge separation ability at the perovskite/HTM interface. The passivation effect is studied by doing a space-charge-limited current (SCLC) analysis. The obtained results are as follows where: VTFL(spiro-OMeTAD) = 0.023 V and VTFL(CuP) = 0.017 V. The trap densities were found to be: Ntrap(spiro-OMeTAD) = 1.11 x 10^{15} cm^{-3} and Ntrap(CuP) = 0.82 x 10^{15} cm^{-3}.

The trap density value can be calculated by using the following relation:

$$V_{TFL} = qN_{trap}d^2/2\varepsilon\varepsilon o$$

The above values clearly show that CuP has strong passivation capability, reducing the traps to produce better performing devices.

To test the reproducibility of the CuP devices, 30 PSCs using CuP and spiro-OMeTAD as HTMs. CuP devices showed good reproducibility by having an average PCE of 17.27%, and spiro-OMeTAD devices had an average PCE of 17.64%, with the best efficiency of 18.61% for 30 devices. Lastly, CuP and spiro-OMeTAD were stored in a room N2 environment at 65% RH and AM 1.5G illumination to test the stability. After 100 hours, the CuP device showed excellent thermal stability by retaining 90% of its initial efficiency. In contrast, the spiro-OMeTAD device retained only 10% of its initial efficiency. Additionally, CuP-based PSCs possessed better moisture and illumination stability. These superior qualities of Cu porphyrins show that these PSCs are closer to commercialization.

2.16 CuI doped PEDOT: PSS double HTM

PEDOT: PSS is a commonly used HTM in PSCs. However, its hygroscopicity and acidic nature question this material's long-term stability as an HTM in PSCs. P-type inorganic materials like CuI, CuO, NiO, and metal oxides were used as alternatives with improved stability and conductivity [61-65]. However, the PCE of these devices are comparatively lower than organic materials due to the poor interfacial contact between the HTM and perovskite is poor. CuI is a favorable alternative because of its high hole mobility, wide bandgap (3.1 eV), hydrophobicity, low cost, eco-friendly, and solution processibility. Devices that have employed CuI in the past have reported higher stability, lower hysteresis, and reduced PCE when compared to spiro-OMeTAD [66,67]. In recent studies, CuI used as an HTM in inverted PSCs had a PCE of 16.8% with improved stability compared to PEDOT: PSS devices. Wei-Dong Hu and co-workers have fabricated a device using a CuI/PEDOT: PSS double HTM and correspondingly obtained the photovoltaic performance. The device is of the configuration ITO/CuI/PEDOT: PSS/MAPbI3/PC61BM/ZnO [68]. Figure 12 is the energy band alignment and device architecture of the above-mentioned device configuration.

The energy band alignment of CuI with PEDOT: PSS was appropriate, thus ensuring suitable hole transfer. Moreover, the position of the CuI conduction band indicates efficient electron blocking. To conduct a comparative analysis, the CuI/PEDOT: PSS film was compared with PEDOT: PSS, CuI,

PEDOT:PSS/CuI film-based devices. The determined optimal thickness was 20 nm, 40 nm, 300 nm, 50 nm, and 40 nm for CuI, PEDOT: PSS, $MAPbI_3$, PC61BM, and ZnO layers. The CuI/PEDOT: PSS device had the highest photovoltaic performance with a J_{sc} = 20.5 mA/cm^2, V_{oc} = 0.92 V, FF = 76% and PCE = 14.3%. PEDOT:PSS-based device gave an output of V_{oc} = 0.86 V, J_{sc} = 20.5 mA/cm^2, FF = 73% and PCE = 12.9%. From comparing the above two devices, it is evident that using CuI as a buffer layer will improve photovoltaic performance greatly. Inverting the double HTM (PEDOT: PSS/CuI) gives an output of, V_{oc} = 0.78 V, J_{sc} = 19.4 mA/cm^2, FF = 68% and PCE = 10.8%. The single CuI device showed the poorest performance with V_{oc} = 0.78 V, J_{sc} = 7.4 mA/cm^2, FF = 30% and PCE = 1.7%. On studying the quantum efficiency spectra, the CuI/PEDOT: PSS-based device showed good performance (>60%) for 360 nm to 750 nm, with the best EQE measurement of nearly 80%. Analyzing the optical transmission spectra of HTM/ITO architecture, we see an absorption peak at 450 nm for CuI. The CuI buffer layer reduces the transmittance, particularly near the 405 nm range, where reduced light intensity reaches the perovskite. This shows that CuI/PEDOT: PSS has improved electrical properties to limit excessive optical losses. The SEM images of different HTMs show that the CuI/PEDOT: PSS and PEDOT: PSS film had similar morphology and surface coverage, with an average grain size of 100 nm. However, the double HTM forms a more dense, compact, and homogeneous film that can be the major reason for higher Voc. The XRD patterns were studied of all the HTMs and perovskites on the substrate. The ITO/PEDOT: PSS architecture showed similar diffraction spectra to ITO due to the amorphous nature of PEDOT: PSS. Similarly, CuI showed a diffraction peak at 25.5° because of the reflection of γ- CuI with the Zincblende FCC structure. However, the diffraction peaks were minimized after the perovskite layer was deposited on CuI.

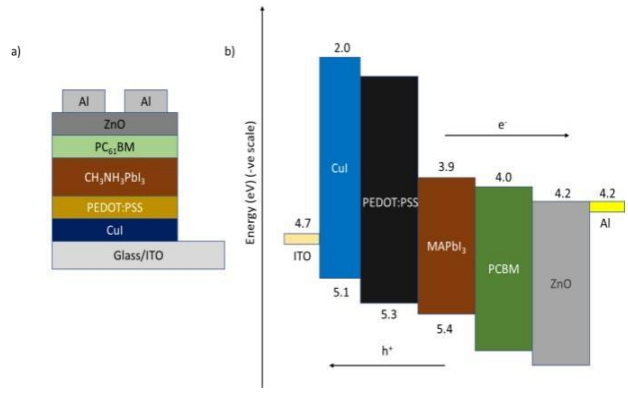

Figure 12. a) PSC Device Structure, b) Energy Band alignment of the device

The PL quenching was observed to be more efficient for CuI/PEDOT: PSS layer. The reduced PL intensity indicates the lower recombination rates at the perovskite/HTM interface. The calculated T_2 values were found to be 23, 17, 13, and 2.7 for CuI, PEDOT: PSS, PEDOT: PSS/CuI, and CuI/PEDOT: PSS, respectively. The long lifetime for CuI shows the poor interfacial contact between the perovskite and HTM. However, observing the lifetime of CuI/PEDOT: PSS we see the lowest value, which indicates the effective hole extraction and transportation ability, reduced radiative recombination, and improved interfacial contact with the perovskite layer. The acidic and hydrophilic nature of PEDOT: PSS is detrimental to the device's long-term stability. Instead, using a double HTM like CuI/PEDOT: PSS can prove a better option because of its excellent stable and hydrophobic nature. The stability of the devices was tested. After 720 hours of storage, the PCE of PEDOT: PSS-based retained only 72% of its initial PCE, whereas CuI/PEDOT: PSS retained 88%. This PCE retaining ability can directly relate to the FF and Jsc values. The corrosive nature of PEDOT: PSS affects the ITO substrate to a great extent. Thus, using a CuI buffer layer can improve the performance and improve the device's operational stability.

2.17 Copper Sulfide Nanoparticles as HTM

In addition to the instability issues associated with PSCs, the high costs of conventional HTMs and low hole mobility require additives or suitable chemical modifications that can provide the HTMs and PSCs with the desired properties to perform efficiently. Typically, the addition of hygroscopic additives like Cobalt and Lithium salts have depicted significant improvement for PSCs. However, these materials accelerate the chemical degradation of the device. Thus, the following research endeavor includes exploring and discovering stable, efficient, and low-cost HTMs that can prove to be a candidate for mass commercialization. Materials like CuI, CuSCN, Carbon Nanotubes, CIGSSe, NiO, etc., have been considered possible candidates. However, many materials require high processing temperatures to crystallize properly [69-72]. Additionally, many of these materials are even fabricated in polar solvents. This manufacturing method can deteriorate the perovskite film in an n-i-p configuration. In a recent report, the usage of CuSCN was reported to give a PCE of 16% in an n-i-p configuration, which further improved to 20.2% upon certain modifications [73]. However, these films were produced through toxic solvents like diethyl sulfide, which further limits the commercialization of the device. In this section, Juan Tirado and coworkers developed a $Cu_{2-x}S$ film with x varying from 0 to 1. It was shown that among the various combinations of $Cu_{2-x}S$, the covellite form (CuS) has the highest concentration of valence-band-delocalized holes, typically showing the highest p-type characteristics for a suitable HTM. Moreover, CuS has also been used previously for various optoelectronic devices. The principal reason hindering the usage of CuS as an HTM is the lack of compatibility with a precursor solution, the high processing temperatures, and the toxic materials used [74, 75]. However, in this section, Juan Tirado and coworkers have successfully fabricated CuS nanoparticles as a fully-functional HTM in non-polar solvents, with low costs and stabilized form [76]. The produced particles are found to be compatible in inverted and direct configurations. Through Juan Tirado and co-workers' activities, two devices were fabricated using $MAPbI_3$ and CsFAMAPbIBr using the architecture: FTO/c-TiO_2/m-TiO_2/Perovskite/CuS/Au.

The CuS nanoparticles were prepared through a modified process where a non-polar solvent was used for its fabrication. The process involved two precursor solutions, namely, sulfur powder and copper chloride, dissolved in oleylamine. The copper chloride precursor solution was

heated to 150oC. The sulfur powder precursor solution was added rapidly to form CuS nanoparticles in a rapid reaction collected and dispersed in toluene. The XRD measurements show diffraction peaks at 27.21°, 29.36°, 32.35°, 33.52°, 48.09°, 52.33°, and 59.05°. All these peaks correspond to the hexagonal phase of CuS. There were no additional peaks of various Cu:S ratios, indicating that only the CuS phase was present in its entirety. The TEM analysis was conducted to analyze the morphology of the film. The CuS nanocrystals show a 2-D disc-shaped orientation with a size of 20 nm and a thickness of 4 nm. There are two intense Raman active phonon modes at nearly 60 and 475/cm. These can be attributed to the S-S vibrational modes that provide an added support for CuS formation. The XPS analysis shows three voltage bands located at 932.8, 162.59, and 163.77 eV, corresponding to Cu $2p_{3/2}$, S $2p_{1/2}$, and S $2p_{3/2}$ planes. Using XPS measurements, with slight modifications and extensive analysis, we can observe a trace amount of Cu (II) present instead of Cu (I). The XPS results provide a rough estimation of the optical bandgap of CuS to be around 2.4 eV and a single intense extinction band at wavelengths above 900 nm (NIR). This reveals the plasmonic-semiconductor dual nature. The devices using $MAPbI_3$ and CsFAMAPbIBr were fabricated using different spin-coating speeds of CuS to evaluate the superior deposition speed required for optimum performance. A distinct feature spotted is that the optimal speed required for maximum performance varies depending on the active perovskite layer. This can be related to the surface roughness difference of the film and film compatibility in the entire device. The SEM images show that the films produced with $MAPbI_3$ and CsFAMAPbIBr are smooth, compact, and dense films. The thickness of the CuS layer accordingly varied with 55 nm for MAPbI3 and 120 nm for CsFAMAPbIBr-based devices, respectively. The PCE obtained was nearly 13.5 % and 12% for $MAPbI_3$ and CsFAMAPbIBr devices. These values were then compared to PSCs without HTMs. They showed deficient performance in both the cases (<1%), thus confirming the positive impact of CuS as an HTM. The hysteresis phenomenon could not be avoided. This can be related to the perovskite ion migration within the cell, which causes charge accumulation within the device, particularly near the interfacial regions of the perovskite/charge transport layer. Table 8 is a distinct representation of varying photovoltaic performance with spinner speed. It is important to note that the table highlights the photovoltaic performance of two different perovskites (inorganic and mixed). The stability of the devices was evaluated under 40% RH at 20°C under ambient conditions. In the case of $MAPbI_3$, the cell began to degrade rapidly after 192 hours, and CsFAMAPbIBr could retain 80% of its initial PCE. This PCE-retaining ability was also obtained when Spiro-OMeTAD was used as the HTM for the CsFAMAPbIBr device. However, in the latter case, the addition of additives and doping agents degraded the device's performance due to the hygroscopic nature of the dopants, which eventually absorbed a significant amount of moisture. The efficiencies obtained in both cases are nearly comparable to conventional devices. The critical aspect is that low-temperature processing and appropriate precursor solution selection can produce compact and efficient films and devices. The V_{oc} values obtained were nearly 0.89 V for $MAPbI_3$, which decreased to nearly 0.74 V for CsFAMAPbIBr. The V_{oc} values obtained were lesser than the Spiro-OMeTAD-based device (~1.0 V). The valence band spectrum intensity is extended to the Fermi level.

Table 8. Photovoltaic performance using CuS, Spiro-OMeTAD and without HTM, along with varying spinner speed

Spinner Speed	V_{oc} (V)	J_{sc} (mA/cm²)	FF	PCE (%)
$CH_3NH_3PbI_3$ perovskite				
without HTM	0.57	1.07	0.69	0.42
3000	0.82	20.46	0.62	10.45
3500	0.87	20.92	0.69	12.49
4000	0.88	20.72	0.71	13.01
4500	0.83	19.83	0.69	11.39
Spiro-OMeTAD	1.04	21.77	0.74	16.98
$(FAPbI_3)_{0.78}$ $(MAPbI_3)_{0.14}$ $(CsPbI_3)_{0.08}$ perovskite				
without HTM	0.42	8.16	0.48	1.64
1000	0.72	21.57	0.73	11.37
1500	0.75	21.23	0.74	11.72
2000	0.73	19.95	0.71	10.33
2500	0.71	20.91	0.69	10.35
3000	0.73	20.29	0.68	10.15
Spiro-OMeTAD	0.92	21.95	0.76	15.27

We can identify a low density of states (DOS) at the Fermi level on closer analysis. This same feature is what provides CuS nanoparticles with a slightly metallic character. Using UPS measurements, the energy band alignment of the films is studied. The filled-up DOS to the Fermi level and the CBM under the optical bandgap of 2.4 eV show the compatibility of CuS as an HTM with appropriate electron blocking capability. However, there is a considerable energy gap between $MAPbI_3$ (5.61 eV) and CsFAMAPbIBr (5.71 eV) and the VBM of CuS (4.61 eV) of nearly 1.2 eV. This considerable energy gap can allow electron-hole recombination, particularly at the HTM/perovskite interface. However, in this case, the trim work function between TiO_2 and CuS of 0.6 eV still provides a comparatively higher V_{oc}. The PL measurements are taken to study the charge transfer dynamics. It is important to note that PL analysis does not give a detailed analysis of all the charge transfer mechanisms within the device and often limits the analysis between the perovskite/charge transporting material interface. The first case of PL measurements is conducted to understand radiative combination. The quenching intensity is studied concerning the Spiro-OMeTAD device. At V_{oc} conditions, the reference

device shows nearly two times the intensity of the CuS-based devices. Thus, for the same thickness of the HTM, CuS shows a lower V_{oc} value due to non-radiative recombination. Despite the more prominent probability of non-radiative recombination, there is a significant amount of charge transfer, separation, and collection. On further analyzing the device under UPS measurements under light exposure, a redshift of 0.7 eV is observed for the work function and valence band, which is reversible upon light removal. This effect is mainly due to the metallic character of CuS nanoparticles, which provides the material with a hole-injection characteristic and an electrode-like nature lying adjacent to the perovskite. When devices are exposed to light, there is an immediate generation of charge carriers where holes are efficiently extracted and collected by CuS to create a space charge up to the sample surface. Thus, the energy shift is directly proportional to the V_{oc} values, which further depends on the metallic character of CuS nanoparticles. The flake-shaped CuS nanoparticles have been fabricated through low-temperature processing methods, stabilized using non-polar solvents, and compatible with organic-inorganic perovskite layers. The performance of these materials is comparable to the conventional PSCs we use today. However, the V_{oc} values are comparatively lower. This can be eradicated using a suitable interlayer or appropriate interface engineering between the perovskite/CuS interface, potentially reducing the energy gap. However, such an innovation allows further improvements and applications where low-temperature PSCs can be processed for a large-scale setup.

3. Conclusions

The article presses on how vital hole and electron transport can be, especially in the performance of a PSC. To optimize the performance of a device from a charge transport point of view, the interface between the ETM or HTM and perovskite should be as complementary as possible. Moreover, modifying the structural aspects of molecules by either molecular engineering or suitable growth mechanisms can contribute to charge transport. Lastly, doping or using certain additives helps in tuning the physical and chemical properties of the charge transport layer, making it suitable for high device performance. Coming to the case of Bi and Cu-based PSCs, these innovations have a lot of scopes ahead. We need to consider improving film quality, regulating the crystallization process, varying the deposition techniques, paying attention to certain materials that can tune bandgap levels, and developing materials to behave as inter-layers or buffer layers. These, in turn, yield more extraordinary device performance and produce high-efficiency light-harvesting systems. Through this review, we could comprehend the various innovations in the Perovskite Solar Cell industry. Typically, to replace the inefficient and conventional HTMs and ETMs that we use today, we aim to develop more coherent, compact, organic, and efficient films that can be considered future possibilities for commercialization. Moreover, the review delves into the various strategies that remarkable researchers have used to replace the Pb-toxicity in PSCs using Bi and Cu-based substitutions or modifications. The comprehensive tactics that have been used to produce highly efficient PSCs and the future works that can be carried out to improve further and remove the limitations that the existing methods carry are of utmost importance. The Perovskite Solar Cell industry and research are highly in-demand. The scope for research and study is vastly extensive, which can pave the way for the next big thing to manufacture these devices on a large scale and for various applications.

Ethical issue

The author is aware of and complies with best practices in publication ethics, specifically with regard to authorship (avoidance of guest authorship), dual submission, manipulation of figures, competing interests, and compliance with policies on research ethics. The author adheres to publication requirements that the submitted work is original and has not been published elsewhere in any language.

Data availability statement

Data sharing is not applicable to this article as no datasets were generated or analyzed during the current study.

Conflict of interest

The author declares no potential conflict of interest.

References

[1] Jin, J., Yang, M., Deng, W., Xin, J., Tai, Q., & Qian, J. et al. (2021). Highly efficient and stable carbon-based perovskite solar cells with the polymer hole transport layer. Solar Energy, 220, 491-497. doi: 10.1016/j.solener.2021.03.081

[2] Chen, H.-B.; Ding, X.-H.; Pan, X.; Hayat, T.; Alsaedi, A.; Ding, Y.; Dai, S.-Y., Incorporating C60 as Nucleation Sites Optimizing PbI2 Films to Achieve Perovskite Solar Cells Showing Excellent Efficiency and Stability Via Vapor-Assisted Deposition Method. ACS Appl. Mater. Interfaces 2018, 10, 2603-2611.

[3] Enhanced Performance and Stability of Planar Perovskite Solar Cells by Interfacial Engineering using Fluorinated Aliphatic Amines Shuai Zhao, Baohua Zhao, Yanli Chen, Guangwu Yang, and Xiyou Li ACS Applied Energy Materials 2019 2 (9), 6230-6236 DOI: 10.1021/acsaem.9b00757

[4] Zhang, L., Zhou, X., Zhong, X., Cheng, C., Tian, Y., & Xu, B. (2019). Hole-transporting layer based on a conjugated polyelectrolyte with organic cations enables efficient inverted perovskite solar cells. Nano Energy, 57, 248-255. doi: 10.1016/j.nanoen.2018.12.033

[5] Tsarev, S., Luchkin, S., Stevenson, K., & Troshin, P. (2020). Perylenetetracarboxylic dianhydride as organic electron transport layer for n-i-p perovskite solar cells. Synthetic Metals, 268, 116497. doi: 10.1016/j.synthmet.2020.116497

[6] J.L. Wu, W.K. Huang, Y.C. Chang, B.C. Tsai, Y.C. Hsiao, C.Y. Chang, C.T. Chen, C.T. Chen, Simple mono-halogenated perylene diimides as non-fullerene electron transporting materials in inverted perovskite solar cells with ZnO nanoparticle cathode buffer layers, J. Mater. Chem. A 5 (2017) 12811–12821.

[7] S.S. Kim, S. Bae, W.H. Jo, A perylene diimide-based non-fullerene acceptor as an electron transporting material for inverted perovskite solar cells, RSC Adv. 6 (2016) 19923–19927.

[8] C. Chen, M. Cheng, H. Li, F. Qiao, P. Liu, H. Li, L. Kloo, L. Sun, Molecular engineering of ionic type perylenediimide dimer-based electron transport materials for efficient planar perovskite solar cells, Mater. Today Energy 9 (2018) 264–270.
[9] G.-H. Kim, H. Jang, Y.-J. Yoon, J. Jeong, S.Y. Park, B. Walker, et al., Fluorine functionalized graphene nano platelets for highly stable inverted perovskite solar cells, Nano Lett. 17 (10) (2017) 6385–6390.
[10] P. Karuppuswamy, C. Hanmandlu, K. Moorthy Boopathi, P. Perumal, Cching Liu, Y.F. Chen, Y.C. Chang, P.C. Wang, C.S. Lai, C.W. Chu, Solution-processable electron transport layer for efficient hybrid perovskite solar cells beyond fullerenes, Sol. Energy Mater. Sol. Cells 169 (2017) 78–85.
[11] F. Bella, G. Griffini, J.-P. Correa-Baena, G. Saracco, M. Gratzel, A. Hagfeldt, et al., Improving efficiency and stability of perovskite solar cells with photocurable fluoropolymers, Science 354 (6309) (2016) 203–206.
[12] H. Liu, M. Wang, J. Bian, Y. Feng, Z. Wang, B. Zhang, et al., Enhanced stability of perovskite solar cells using hydrophobic organic fluoropolymer, Appl. Phys. Lett. 113 (2) (2018), 023902.
[13] Zijun Wang, Dayong Zhang, Genjie Yang, and Junsheng Yu , "Exceeding 19% efficiency for inverted perovskite solar cells used conventional organic small molecule TPD as hole transport layer", Appl. Phys. Lett. 118, 183301 (2021) https://doi.org/10.1063/5.0050512
[14] X. Xu, C. Ma, Y. Chen, Y. M. Xie, X. Yi, B. Gautam, S. Chen, H. W. Li, C. S. Lee, F. So, and S. W. Tsang, J. Power Sources 360, 157 (2017).
[15] X. Liu, Y. Cheng, C. Liu, T. Zhang, N. Zhang, S. Zhang, J. Chen, Q. Xu, J. Quyang, and H. Gong, Energy Environ. Sci. 12, 1622 (2019).
[16] J. Yang, C. Liu, C. Cai, X. Hu, Z. Huang, X. Duan, et al., High-performance perovskite solar cells with excellent humidity and thermo-stability via fluorinated perylenediimide, Adv. Energy. Mater. 9 (18) (2019), 1900198.
[17] Malik, H., Ma, L., Luo, J., Xia, J., Wan, Z., & Khan, M. et al. (2020). Novel hole transporting material based on tetrathiafulvalene derivative: A step towards dopant free, ambient stable and efficient perovskite solar cells. Solar Energy, 201, 658-665. doi: 10.1016/j.solener.2020.03.003
[18] Luo, J., Xia, J., Yang, H., Chen, L., Wan, Z., Han, F., Malik, H.A., Zhu, X., Jia, C.Y., 2018. Energy Environ. Sci. 11, 2035–2045.
[19] Luo, J., Xia, J., Yang, H., Malik, H.A., Han, F., Shu, H., Yao, X., Wan, Z., Jia, C.Y., 2020. Nano Energy. 70, 104509.
[20] D. Yang, T. Sano, Y. Yaguchi, H. Sun, H. Sasabe, and J. Kido, Adv. Funct. Mater. 29, 1807556 (2019).
[21] J. Zhang, B. Xu, L. Yang, A. Mingorance, C. Ruan, Y. Hua, L. Wang, N. Vlachopoulos, M. Lira-Cantú, G. Boschloo, A. Hagfeldt, L. Sun and E. M. J. Johansson, Advanced Energy Materials, 2017, 7, 1602736.
[22] 17. C. Huang, W. Fu, C. Z. Li, Z. Zhang, W. Qiu, M. Shi, P. Heremans, A. K. Jen and H. Chen, J Am Chem Soc, 2016, 138, 2528-2531.
[23] Toward ideal hole transport materials: a review on recent progress in dopant-free hole transport materials for fabricating efficient and stable perovskite solar cells, Xinxing Yin, Zhaoning Song, Zaifang Li and Weihua Tang, Energy Environ. Sci., 2020,13, 4057-4086.
[24] N.K. Elumalai, A. Uddin, Hysteresis in organic-inorganic hybrid perovskite solar cells, Sol. Energy Mater. Sol. Cells 157 (2016) 476e509.
[25] Fan Wu, Rajesh Pathak, Chong Chen, Yanhua Tong, Haibin Xu, Tiansheng Zhang, Ronghua Jian, Xiaoyi Li, Qiquan Qiao, Reduced hysteresis in perovskite solar cells using metal oxide/organic hybrid hole transport layer with generated interfacial dipoles, Electrochimica Acta, Volume 354, 2020, 136660, ISSN 0013-4686, https://doi.org/10.1016/j.electacta.2020.136660.
[26] S.N. Habisreutinger, N.K. Noel, H.J. Snaith, Hysteresis index: a figure without merit for quantifying hysteresis in perovskite solar cells, ACS Energy Lett. 3 (2018) 2472e2476.
[27] Z. Chen, J.J. Wang, Y. Ren, C. Yu, Kai Shum, Appl. Phys. Lett. 101 (2012), 093901.
[28] Nakita K. Noel, et al., Lead-free organiceinorganic tin halide perovskites for photovoltaic applications, Energy Environ. Sci. 7 (9) (2014) 3061e3068.
[29] C. Wehrenfennig, M. Liu, H.J. Snaith, M.B. Johnston, L.M. Herz, Homogeneous emission line broadening in the organo lead halide perovskite CH3NH3PbI3xClx, J. Phys. Chem. Lett. 5 (2014) 1300e1306.
[30] Takeo Oku, Crystal Structures of CH3NH3PbI3 and Related Perovskite Compounds Used for Solar Cells, Solar Cells-New Approaches and Reviews, InTech, 2015.
[31] G. Giorgi, K. Yamashita, Alternative, lead-free, hybrid organiceinorganic perovskites for solar applications: a DFT analysis, Chem. Lett. 44 (6) (2015) 826e828.
[32] Ismail Benabdallah, Mourad Boujnah, Abdallah El Kenz, Abdelilah Benyoussef, Mohamed Abatal, Ali Bassam, Lead-free perovskite based bismuth for solar cells absorbers, Journal of Alloys and Compounds, Volume 773, 2019, Pages 796-801, ISSN 0925-8388, https://doi.org/10.1016/j.jallcom.2018.09.332.
[33] T. Singh, A. Kulkarni, M. Ikegami, T. Miyasaka, ACS Appl. Mater. Interfaces 8, 14542 (2016).
[34] B.-W. Park, B. Philippe, X. Zhang, H. Rensmo, G. Boschloo, E. M. J. Johansson, Adv. Mater. 27, 6806 (2015).
[35] Sanders, S., Stümmler, D., Pfeiffer, P., Ackermann, N., Simkus, G., Heuken, M., . . . Kalisch, H. (2018). Fabrication and Characterization of Air-Stable Organic-Inorganic Bismuth-Based Perovskite Solar Cells. MRS Advances, 3(51), 3085-3090. doi:10.1557/adv.2018.514
[36] B. Chen, H. Hu, T. Salim, Y.M. Lam, A facile method to evaluate the influence of trap densities on perovskite solar cell performance, J. Mater. Chem. C 7 (19) (2019) 5646–5651, https://doi.org/10.1039/C9TC00816K.
[37] W. Nie, H. Tsai, R. Asadpour, J.-C. Blancon, A.J. Neukirch, G. Gupta, J.J. Crochet, M. Chhowalla, S. Tretiak, M.A. Alam, H.-L. Wang, A.D. Mohite, High-efficiency solution-processed perovskite solar cells with millimeter-scale grains, Science 347 (6221)

(2015) 522–525, https://doi.org/10.1126/science:aaa0472.
[38] B.-M. Bresolin, S.B. Hammouda, M. Sillanpää, Methylammonium iodo bismuthate perovskite (CH3NH3)3Bi2I9 as new effective visible lightresponsive photocatalyst for degradation of environment pollutants, J. Photochem. Photobiol., A 376 (2019) 116–126, https://doi.org/10.1016/j.jphotochem.2019.03.009.
[39] A. Kojima, K. Teshima, Y. Shirai, T. Miyasaka, Organometal Halide Perovskites as Visible-Light Sensitizers for Photovoltaic Cells, J. Am. Chem. Soc. 131 (17) (2009) 6050–6051, https://doi.org/10.1021/ja809598r.
[40] Muhd Sahrul Nizam Sahul Hameed, Farhana Aziz, Solvent engineering of lea free bismuth-based perovskite material for potential application of solar cell, Materials Today: Proceedings, Volume 46, Part 5, 2021, Pages 1837-1842, ISSN 2214-7853, https://doi.org/10.1016/j.matpr.2020.11.1018.
[41] a) T. Krishnamoorthy, H. Ding, C. Yan, W. L. Leong, T. Baikie, Z. Zhang, M. Sherburne, S. Li, M. Asta, N. Mathews, S. G. Mhaisalkar, J. Mater. Chem. A 2015, 3, 23829; b) F. Hao, C. C. Stoumpos, D. H. Cao, R. P. H. Chang, M. G. Kanatzidis, Nat. Photonics 2014, 8, 489; c) M. H. Kumar, S. Dharani, W. L. Leong, P. P. Boix, R. R. Prabhakar, T. Baikie, C. Shi, H. Ding, R. Ramesh, M. Asta, M. Graetzel, S. G. Mhaisalkar, N. Mathews, Adv. Mater. 2014, 26, 7122.
[42] S. Shao, J. Liu, G. Portale, H. H. Fang, G. R. Blake, G. H. t. Brink, L. J. A. Koster, M. A. Loi, Adv. Energy Mater. 2018, 8, 1702019.
[43] P. C. Harikesh, H. K. Mulmudi, B. Ghosh, T. W. Goh, Y. T. Teng, K. Thirumal, M. Lockrey, K. Weber, T. M. Koh, S. Li, S. Mhaisalkar, N. Mathews, Chem. Mater. 2016, 28, 7496
[44] H. Robert, B. Riley, O. Anna, S. Vladan, S. Samuel, W. Mark, K. Hyunho, A. Austin, P. John, K. Rachel, P. Jeremy, W. Evelyn, B. Moungi, B. Vladimir, B. Tonio, Chem. Eur. J. 2016, 22, 2605
[45] M. Lyu, J.-H. Yun, M. Cai, Y. Jiao, P. V. Bernhardt, M. Zhang, Q. Wang, A. Du, H. Wang, G. Liu, L. Wang, Nano Res. 2016, 9, 692
[46] B.-W. Park, B. Philippe, X. Zhang, H. Rensmo, G. Boschloo, E. M. J. Johansson, Adv. Mater. 2015, 27, 6806.
[47] B. Ghosh, S. Chakraborty, H. Wei, C. Guet, S. Li, S. Mhaisalkar, N. Mathews, J. Phys. Chem. C 2017, 121, 17062; b) B. Ghosh, B. Wu, H. K. Mulmudi, C. Guet, K. Weber, T. C. Sum, S. G. Mhaisalkar, N. Mathews, ACS Appl. Mater. Interfaces 2018.
[48] Y. Kim, Z. Yang, A. Jain, O. Voznyy, G.-H. Kim, M. Liu, L. N. Quan, F. P. García de Arquer, R. Comin, J. Z. Fan, E. H. Sargent, Angew. Chem. 2016, 128, 9738.
[49] H. Zhu, M. Pan, M. B. Johansson, E. M. J. Johansson, ChemSusChem 2017, 10, 2592.
[50] Ghosh, B., Wu, B., Guo, X., Harikesh, P., John, R., & Baikie, T. et al. (2018). Superior Performance of Silver Bismuth Iodide Photovoltaics Fabricated via Dynamic Hot-Casting Method under Ambient Conditions. Advanced Energy Materials, 8(33), 1802051. doi: 10.1002/aenm.201802051
[51] Zhang F, Yang X, Cheng M, Wang W, Sun L. Boosting the efficiency and the stability of low cost perovskite solar cells by using CuPc nanorods as hole transport material and carbon as counter electrode. Nano Energy 2016;20: 108e16.
[52] Ke W, Zhao D, Grice CR, Cimaroli AJ, Fang G, Yan Y. Efficient fully-vacuum processed perovskite solar cells using copper phthalocyanine as hole selective layers. J Mater Chem A 2015;3:23888e94.
[53] Cho KT, Rakstys K, Cavazzini M, Orlandi S, Pozzi G, Nazeeruddin MK. Perovskite solar cells employing molecularly engineered Zn(II) phthalocyanines as hole-transporting materials. Nano Energy 2016. http://dx.doi.org/10.1016/j.nanoen.2016.09.008.
[54] Yang G, Wang YL, Xu JJ, Lei HW, Chen C, Shan HQ, et al. A facile molecularly engineered copper (II) phthalocyanine as hole transport material for planar perovskite solar cells with enhanced performance and stability. Nano Energy 2016. http://dx.doi.org/10.1016/j.nanoen.2016.11.039.
[55] Liu, X., Wang, Y., Rezaee, E., Chen, Q., Feng, Y., & Sun, X. et al. (2018). Tetra-Propyl-Substituted Copper (II) Phthalocyanine as Dopant-Free Hole Transporting Material for Planar Perovskite Solar Cells. Solar RRL, 2(7), 1800050. doi: 10.1002/solr.201800050
[56] S. Wang, W. Yuan, Y.S. Meng, ACS Appl. Mater. Interf. 7 (2015) 24791, https://doi.org/10.1021/acsami.5b07703.
[57] M. Freitag, Q. Daniel, M. Pazoki, K. Sveinbjörnsson, J.B. Zhang, L. C. Sun, A. Hagfeldt. G. Boschloo. Energy Environ. Sci. 8, 2634 (2015). https://doi.org/ 10. 1039/C5EE01204J.
[58] Y.M. Cao, Y. Saygili, A. Ummadisingu, J. Teuscher, J.S. Luo, N. Pellet, F. Giordano, S.M. Zakeeruddin, J.-E. Moser, M. Freitag, A. Hagfeldt, M. Grätzel, Nat. Commun. 8 (2017) 15390, https://doi.org/10.1038/ncomms15390.
[59] S. Chen, P. Liu, Y. Hua, Y.Y. Li, L. Kloo, X.Z. Wang, B. Ong, W.K. Wong, X.J. Zhu, ACS Appl. Mater. Interfaces 9 (2017) 13231, https://doi.org/10.1021/acsami.7b01904.
[60] Chang-Dai Si, Xu-Dong Lv, Shi-Jia Long, Perovskite solar cells employing copper (I/II) porphyrin hole-transport material with enhanced performance, Inorganic Chemistry Communications, Volume 112, 2020, 107701, ISSN 1387-7003, https://doi.org/10.1016/j.inoche.2019.107701.
[61] M.I. Hossain, F.H. Alharbi, N. Tabet, Copper oxide as inorganic hole transport material for lead halide perovskite based solar cells, Sol. Energy 120 (2015) 370–380.
[62] K.C. Wang, P.S. Shen, M.H. Li, S. Chen, M.W. Lin, P. Chen, T.F. Guo, Low- temperature sputtered nickel oxide compact thin film as effective electron blocking layer for mesoscopic NiO/CH3NH3PbI3 perovskite heterojunction solar cells, ACS Appl. Mater. Interfaces 6 (2014) 11851–11858.
[63] V. Trifiletti, V. Roiati, S. Colella, R. Giannuzzi, L. De Marco, A. Rizzo, M Manca, A. Listorti, G. Gigli,

NiO/MAPbI(3-x)Cl(x)/PCBM. a model case for an improved understanding of inverted mesoscopic solar cells, ACS Appl. Mater. Interfaces 7 (2015) 4283–4289.
[64] W. Sun, S. Ye, H. Rao, Y. Li, Z. Liu, L. Xiao, Z. Chen, Z. Bian, C. Huang, Room-temperature and solution-processed copper iodide as the hole transport layer for inverted planar perovskite solar cells, Nanoscale 8 (2016) 15954–15960.
[65] D.Y. Lee, S.I. Na, S.S. Kim, Graphene oxide/PEDOT:PSS composite hole transport layer for efficient and stable planar heterojunction perovskite solar cells, Nanoscale 8 (2016) 1513–1522.
[66] J.A. Christians, R.C.M. Fung, P.V. Kamat, An inorganic hole conductor for organo-lead halide perovskite solar cells. improved hole conductivity with copper iodide, J. Am. Chem. Soc. 136 (2014) 758–764.
[67] G.A. Sepalage, S. Meyer, A. Pascoe, A.D. Scully, F.Z. Huang, U. Bach, Y.B. Cheng, L. Spiccia, Copper(I) iodide as hole-conductor in planar perovskite solar cells: probing the origin of J-V hysteresis, Adv. Funct. Mater. 25 (2015) 5650–5661.
[68] Wei-Dong Hu, Chunxiang Dall'Agnese, Xiao-Feng Wang, Gang Chen, Meng-Zhen Li, Jia-Xing Song, Ying-Jin Wei, Tsutomu Miyasaka, Copper iodide-PEDOT:PSS double hole transport layers for improved efficiency and stability in perovskite solar cells, Journal of Photochemistry and Photobiology A: Chemistry, Volume 357, 2018, Pages 36-40, ISSN 1010-6030, https://doi.org/10.1016/j.jphotochem.2018.02.018.
[69] N.-G. Park, Perovskite solar cells: an emerging photovoltaic technology, Mater. Today 18 (2015) 65–72, https://doi.org/10.1016/j.mattod.2014.07.007.
[70] P. Qin, S. Tanaka, S. Ito, N. Tetreault, K. Manabe, H. Nishino, M.K.Nazeeruddin, M. Grätzel, Inorganic hole conductor-based lead halide perovskite solar cells with 12.4% conversion efficiency, Nat Commun. 5 (2014), https://doi.org/10.1038/ncomms4834.
[71] Z. Liu, A. Zhu, F. Cai, L. Tao, Y. Zhou, Z. Zhao, Q. Chen, Y.-B. Cheng, H. Zhou, Nickel oxide nanoparticles for efficient hole transport in p-i-n and n-i-p perovskite solar cells, J. Mater. Chem. A 5 (2017) 6597–6605, https://doi.org/10.1039/C7TA01593C.
[72] M.I. Hossain, F.H. Alharbi, N. Tabet, Copper oxide as inorganic hole transport material for lead halide perovskite based solar cells, Sol. Energy 120 (2015) 370–380, https://doi.org/10.1016/j.solener.2015.07.040.
[73] N. Arora, M.I. Dar, A. Hinderhofer, N. Pellet, F. Schreiber, S.M. Zakeeruddin, M. Grätzel, Perovskite solar cells with CuSCN hole extraction layers yield stabilized efficiencies greater than 20%, Science 80 (2017) (2017), https://doi.org/10.1126/science.aam5655.
[74] W. Ke, G. Fang, H. Lei, P. Qin, H. Tao, W. Zeng, J. Wang, X. Zhao, An efficient and transparent copper sulfide nanosheet film counter electrode for bifacial quantum dot-sensitized solar cells, J. Power Sources 248 (2014) 809–815, https://doi.org/10.1016/j.jpowsour.2013.10.028.
[75] K.-J. Huang, J.-Z. Zhang, Y. Fan, One-step solvothermal synthesis of different morphologies CuS nanosheets compared as supercapacitor electrode materials, J. J. Tirado et al. Applied Surface Science 478 (2019) 607–614 Alloys Compd. 625 (2015) 158–163, https://doi.org/10.1016/j.jallcom.2014.11.137.
[76] Juan Tirado, Cristina Roldán-Carmona, Fabio A. Muñoz-Guerrero, Gemay Bonilla-Arboleda, Maryline Ralaiarisoa, Giulia Grancini, Valentin I.E. Queloz, Norbert Koch, Mohammad Khaja Nazeeruddin, Franklin Jaramillo,